Resource

Immunity

Spatiotemporal dynamics of CXCL10 encode contextual immune information revealed by the genetically encoded fluorescent sensor

Graphical abstract

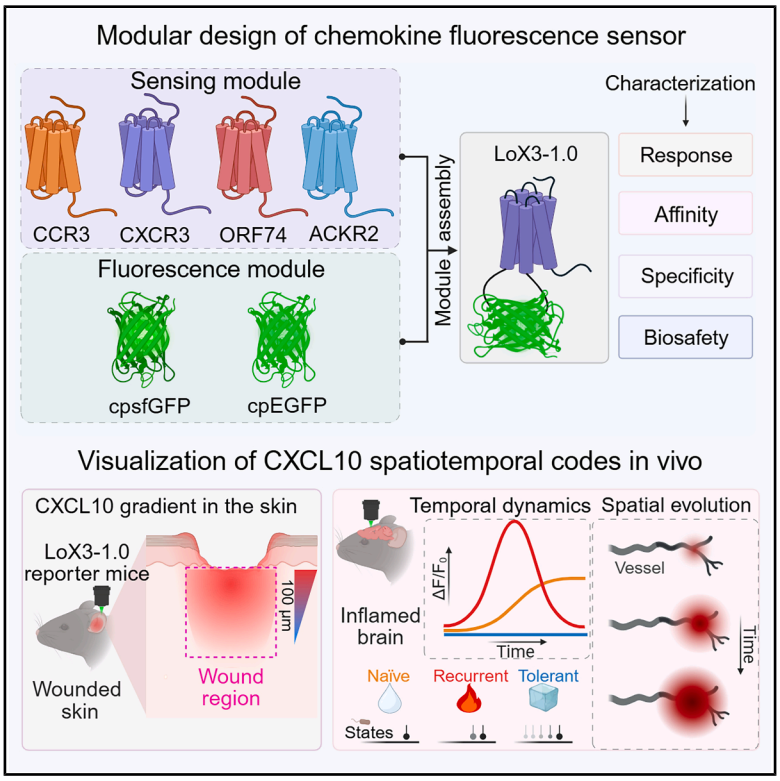

Authors

Fengxue Xi, Chenyu Wang, Yuanxia Wang, ..., Qingchun Guo, Ting Chen, Miao Jing

Correspondence

jingmiao@cibr.ac.cn

In brief

Chemokines are essential signals that coordinate immune responses, yet how they are organized in time and space to convey information remains incompletely understood. Xi et al. develop a genetically encoded CXCL10 sensor, LoX3-1.0, to visualize the state-specific CXCL10 dynamics across multiple systems, revealing how its spatiotemporal features translate environmental information during inflammation.

Highlights

- A genetically encoded fluorescent sensor enables *in vivo* imaging of CXCL10 dynamics
- Multidimensional chemokine patterns encode immune environmental information
- Skin injury induces micrometer-scale CXCL10 gradients near the wound boundary
- Neuroinflammation states drive the spatiotemporal evolution of CXCL10 around vessels

Xi et al., 2025, Immunity *58*, 2320–2335
September 9, 2025
https://doi.org/10.1016/j.immuni.2025.07.005

CellPress

CellPress
OPEN ACCESS

Immunity

Resource

Spatiotemporal dynamics of CXCL10 encode contextual immune information revealed by the genetically encoded fluorescent sensor

Fengxue Xi,[1,2,3,8] Chenyu Wang,[1,2,3,8] Yuanxia Wang,[1,2,3] Pengwei Luan,[2,3,4] Yue Chen,[2,3] Luqiao Tan,[2,3] Nianhan Shang,[2,3] Xinwei Gao,[2,3] Daoming Chen,[5,6] Qingchun Guo,[2,3,7] Ting Chen,[5,6] and Miao Jing[1,2,3,9,*]

[1]Basic Medical Sciences, Capital Medical University, Beijing 100069, China
[2]Beijing Institute for Brain Research, Chinese Academy of Medical Sciences & Peking Union Medical College, Beijing 102206, China
[3]Chinese Institute for Brain Research, Beijing 102206, China
[4]Academy for Advanced Interdisciplinary Studies, Peking University, Beijing 100871, China
[5]National Institute of Biological Sciences, Beijing 102206, China
[6]Tsinghua Institute of Multidisciplinary Biomedical Research, Tsinghua University, Beijing 100084, China
[7]School of Biomedical Engineering, Capital Medical University, Beijing 100069, China
[8]These authors contributed equally
[9]Lead contact
*Correspondence: jingmiao@cibr.ac.cn
https://doi.org/10.1016/j.immuni.2025.07.005

SUMMARY

Chemokines are key extracellular signals that guide cell migration and immune homeostasis, yet how they convey information through their dynamic patterns remains elusive. We engineered a genetically encoded fluorescent sensor, a G protein-coupled receptor (GPCR) activation-based sensor (GRAB)-LoX3-1.0, for the chemokine CXCL10 by inserting a circularly permutated fluorescent protein into the chemokine receptor CXCR3. The sensor exhibited a high signal-to-noise ratio, nanomolar affinity, rapid temporal resolution, and submicrometer spatial resolution that collectively enabled precise mapping of chemokine dynamics. Using LoX3-1.0, we monitored the temporal patterns of chemokines shaped by distinct inflammatory states and quantitatively revealed the multidimensional features of chemokine signaling and its potential organizational principles. *In vivo*, we directly visualized micrometer-scale CXCL10 gradients and their evolution surrounding blood vessels during brain neuroinflammation and also tracked the injury-induced CXCL10 dynamics in the peripheral skin of mice. Collectively, LoX3-1.0 enabled direct visualization of CXCL10 spatiotemporal organization, which functions as context-specific signaling codes conveying environmental information across inflammatory states.

INTRODUCTION

Cells navigate their microenvironments by decoding guidance cues that are themselves tightly controlled in spatiotemporal scales.[1] Precise cell positioning at the right time and place is fundamental for organismal development and immune responses. Among these cues, chemokines play central roles by directing effector cell migration via corresponding receptors,[2–4] as evidenced by the disruption of cell migration in chemokine-deficient conditions.[5] Beyond migration, chemokines also show multifaceted functions that influence a broad range of cellular processes, including priming, proliferation, and survival of immune cells,[6–8] highlighting the complexity and specificity in chemokine signaling and function.

While steady-state concentrations of chemokines have been viewed as the primary determinant of their functional potency, their temporally and spatially heterogeneous distribution suggests that additional information may be encoded in their dynamic patterns.[9–12] For instance, the local steepness of a chemokine gradient works synergistically with its absolute concentration to achieve a sufficient signal-to-noise ratio (SNR) in receptor activation and cell migration.[13] Likewise, temporal dynamics of gradients have been implicated in facilitating effective migration,[14] implying a role for temporal coding.[15] The intrinsic properties of chemokines also enable rich modulations, either through transcriptional regulation or by interactions with extracellular factors.[16,17] Migrating cells can even create local chemokine gradients through receptor-mediated internalization, thus achieving directional migration in homogenous chemokine environments.[18,19] Cells also secrete enzymes to cleave chemokines and modify their activities locally.[20,21] Collectively, chemokines undergo intricate regulations that support their dynamic encoding of information in a context-specific manner. Unfortunately, the precise *in vivo* dynamics of chemokines, especially

how they are generated, maintained, and modulated across contexts, remain largely unclear.

A major gap in chemokine research is the lack of methods capable of dynamically tracing chemokine signals with sufficient spatiotemporal resolution. While expression profiling and biochemical assays provide sensitive readouts of chemokine synthesis and presence,[22,23] their principles limit the ability to track chemokine in native tissues. Assays that are based on receptor endocytosis can detect chemokines at the cellular level[24] but are constrained by the kinetics and efficiency of reporter recycling, making it challenging to achieve high temporal resolution and repeatability. Direct fusion of fluorescent proteins or dyes to chemokines can in principle visualize the signal[25,26]; however, such modulations may alter chemokine interactions with receptors and other factors, compromising faithful signal representation. Overall, methods that can accurately capture extracellular chemokine dynamics *in vivo* with sufficient spatiotemporal sensitivity remain urgently needed.

CXCL10 has been extensively characterized in mediating broad functions, including T cell homing, proliferation, and angiogenesis.[7,27,28] Here, we adopted a modular design strategy based on the GRAB sensor engineering principle[29] to select sensor backbones capable of binding CXCL10, assembled them with fluorescent modules from an optimized GRAB sensor, and employed iterative mutagenesis to enhance sensitivity, which culminated in the development of the GRAB-LoX3-1.0 (LoX3-1.0) that faithfully monitors chemokine dynamics with negligible effects on cellular physiology. The genetic encodability of LoX3-1.0 enables its broad application in both a peripheral cutaneous wound model and *in vivo* neuroinflammation studies in the brain. Moreover, by modulating inflammation states, we achieved a multidimensional characterization of chemokine dynamics that elucidates potential principles of signal organization in response to local stimuli. We also visualized an inflammation-induced micrometer-scale CXCL10 gradient and its temporal evolution in the brain parenchyma *in vivo*, revealing a stable gradient slope despite dynamic changes in overall chemokine concentration. Our findings open avenues for investigating the precise regulation and function of CXCL10 in health and disease.

RESULTS

Modular design enables engineering of a genetically encoded CXCL10 sensor

To engineer a genetically encoded fluorescent sensor for chemokine CXCL10, we first revisited the design principles of GPCR-based fluorescent sensors. In principle, these sensors can be viewed as the integration of a sensing module and a fluorescence module, with the latter part replacing the native signaling domain of GPCRs to produce a detectable output upon ligand binding.[30–34] To better leverage the optimized sequences in the fluorescence module of existing GRAB sensors, we adopted a modular design strategy to select multiple CXCL10-binding proteins, including mammalian receptors and viral proteins,[35] as candidate sensing modules and replaced either the third intracellular loop of receptors or the topologically homologous region of viral proteins with the fluorescence module derived from $GRAB_{NE}$.[36] This module was further optimized by substituting the fluorescent protein with various circular-permutated (cp) variants (Figures 1A and S1A). A membrane-targeting mCherry (mCherry-CAAX) was co-expressed in the same construct to better evaluate the brightness and membrane trafficking of candidates (Figure 1B). Among all screened combinations, the human CXCR3-cpGFP exhibited the strongest fluorescence intensity and prominent membrane localization (Figures 1C and S1B) and was selected as the backbone for further optimization.

To improve the performance, a CXCR3-specific agonist, PS372424 (PS), was used to activate the receptor, and the fluorescence at both baseline and after agonist application was captured. The intensity of the GFP channel was divided by that of the reference mCherry channel (G/R) for normalization at the single-cell level, and the relative changes in G/R were annotated as $\Delta F/F_0$. The SNR was also calculated for each candidate (see STAR Methods). Three sequential steps were conducted: (1) truncation of receptor transmembrane loops that undergo the largest conformational changes,[37,38] (2) sequence optimization at the interface between modules, and (3) mutation of critical residues within cpGFP[39,40] (Figures 1D and S1C–S1H). The candidate with the largest response within each step was chosen as the template for further rounds, which eventually reached a candidate with ~200% fluorescence increases to PS, named GRAB-LoX3-1.0, with LoX3 short for ligand of CXCR3. We further mutated the ligand-binding pocket of CXCR3 to construct a mutant control sensor,[41,42] with the W109Q/D112K variant showing correct membrane localization but negligible fluorescence changes to PS and was named as LoX3-mut (Figure 1E; Table S1).

To assess the response of LoX3-1.0 to the endogenous ligands, HEK293T cells expressing LoX3-1.0 (1.0)- or LoX3-mut (mut) were perfused with 1 μM human CXCL10 (hCXCL10), and real-time fluorescence changes were recorded by confocal microscopy. A clear increase in membrane fluorescence was detected in the 1.0-expressing cells, while no significant changes were recorded in mut-expressing cells (Figures 1F, 1G, and S1I). Adjusting the hCXCL10 concentrations revealed the dose-dependent curve of LoX3-1.0 with an apparent EC_{50} of 15 nM and its sensitivity to report hCXCL10 even at 1 nM (Figures 1H and 1I). LoX3-1.0 also responded to the other two endogenous ligands of CXCR3 (hCXCL9 and 11) with comparable activation and efficacy to those of the native receptor[43,44] (Figures S1J and S1K) and was capable of reporting mouse mCXCL9 and mCXCL10 (Figure S1L).

We continued to explore how LoX3-1.0 responds in the complex environment with multiple chemokine ligands and their cleavage variants. Using differential dose-titration experiments, we recorded the additive effect of three ligands (hCXCL9–11) on LoX3-1.0 signals, suggesting that the sensor represents the combinatory chemokine dynamics contributed by the concentrations and affinities of individual ligands (Figures S1M and S1N). Furthermore, hCXCL10 with N-terminal truncation acted as an antagonist on LoX3-1.0, while the C-terminal truncated hCXCL10 retained full agonist activity (Figures S1O and S1P), consistent with their activities on native CXCR3.[21,45] Therefore, LoX3-1.0 is capable of capturing the functional chemokine dynamics that are sensed by endogenous receptors. Consistently, LoX3-1.0 inherited receptor selectivity and did not respond to other chemokines, cytokines, or major neurotransmitters, and

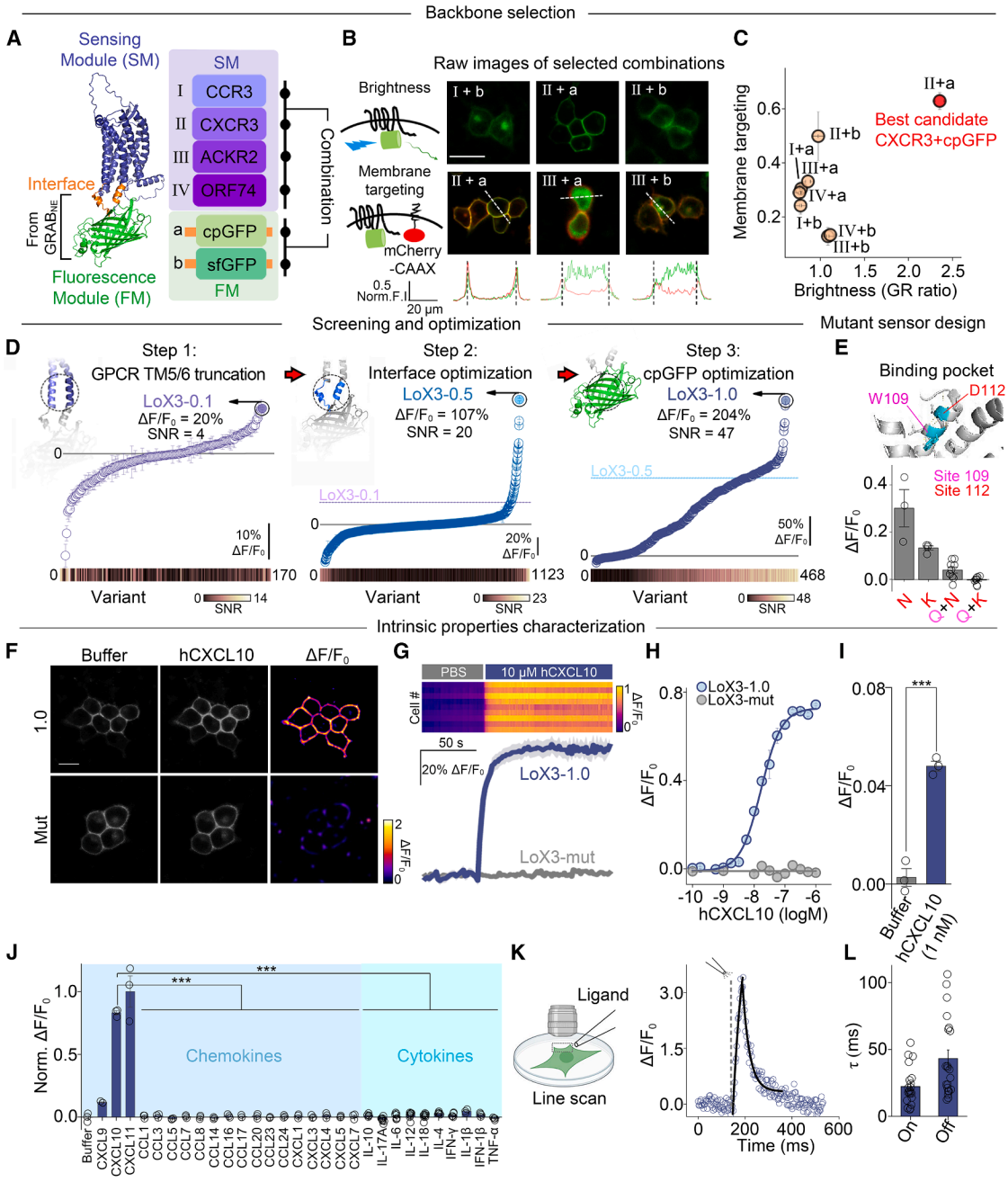

Figure 1. Modular design and optimization of the chemokine sensor LoX3-1.0

(A) Schematic and selected backbones of the modularly designed CXCL10 sensor.

(B) The selection criteria (left) and raw images of candidate sensors with indicated combinations of modules. The fluorescence across white dashed lines is plotted. Additional candidates are summarized in Figures S1A and S1B. Norm.F.I., normalized fluorescence intensity.

(C) The brightness and membrane localization of all combinations (n = 10 fields, each field > 20 cells). The membrane targeting is calculated as the Pearson correlation coefficient of green and red fluorescence.

(D) Iterative sensor optimization based on both the fluorescence response ($\Delta F/F_0$) and signal-to-noise ratio (SNR) to 10 μM PS372424 (PS) (n = 10 fields). Dashed lines indicate the performance of the backbone candidate.

(E) Screening and the performance of the mutant sensor to PS (n = 3, 4, 9, and 9 wells for D112N, D112K, W109Q + D112N, and D112K, respectively).

(F) Images of LoX3-1.0 (up) or LoX3-mut (bottom)-expressing HEK293T cells treated with buffer or human CXCL10 (hCXCL10, 1 μM).

(G) Traces showing the response of LoX3-1.0 or LoX3-mut to hCXCL10 (1 μM) (n = 9 cells).

(H) Dose-dependent responses of LoX3-1.0 or LoX3-mut to hCXCL10 (n = 3 wells, each well > 100 cells).

(I) Quantification of LoX3-1.0 response to buffer or 1 nM hCXCL10 (n = 3 wells).

(J) Quantification of LoX3-1.0 response to various human chemokines and cytokines (at 100 nM; $n \geq 3$ wells).

(legend continued on next page)

also retained pharmacological properties of CXCR3 (Figures 1J and S1Q). The LoX3-1.0 also showed a stable response across physiologically related extracellular pH values and exhibited a similar fluorescent spectrum to EGFP (Figures S1R and S1S). Notably, primary T cells expressing LoX3-1.0 (see STAR Methods) also exhibited dose-dependent fluorescence increase to CXCL10 applications, supporting the sensitivity of LoX3-1.0 when expressed in immune cells (Figures S2A–S2C).

To facilitate quantitative detection of chemokine concentrations, we fused mCherry to the N terminus of LoX3-1.0 for ratiometric measurements (Figures S2D–S2F) and compared the sensor-reported values with standard enzyme-linked immunosorbent assay (ELISA) measurements. The fluorescence response of the sensor (green-to-red ratio) was converted into the amount of hCXCL10 according to the dose-dependent curve obtained in the same system, which showed high consistency with the ELISA results, supporting the ability of LoX3-1.0 to report both the absolute concentrations of CXCL10 and its dynamics (Figure S2G).

LoX3-1.0 captures spatiotemporal differences in CXCL10 patterns

The spatiotemporal resolution of LoX3-1.0 can capture intricate chemokine patterns that may encode rich information. We first examined the intrinsic kinetics of the sensor by locally puffing the agonist PS (100 μM) mixed with a red dye (Figure 1K). LoX3-1.0 exhibited a rapid fluorescence increase with minimal delay (~2 ms) following agonist application and tens of millisecond of kinetics at both the on (18 ms) and off (35 ms) phases (Figures 1L and S2H). Local delivery of hCXCL10 (1 μM) also evoked rapid sensor response (Figure S2I). Prolonged incubation with PS did not alter the off-rate of LoX3-1.0, which supports its robustness and repeatability (Figures S2J–S2L).

Next, we manually generated distinct CXCL10 patterns and tested whether LoX3-1.0 outperformed ELISA methods in reporting spatiotemporal patterns. Temporal patterns with varying numbers and intervals of hCXCL10 applications were locally delivered (see STAR Methods), with continuous solution exchange to mimic the tissue environment. For comparison, solutions at different time points were collected for post hoc ELISA detection (Figure 2A). The fluorescence changes of LoX3-1.0 clearly followed each hCXCL10 application and globally reflected the temporal patterns, with the same time interval between the sensor response and chemokine application (Figure 2B). By contrast, ELISA could only detect the presence of hCXCL10 but exhibited lower resolution and accuracy in reporting patterns, as indicated by the varied peak intervals that deviated from those of the CXCL10 (Figures 2C and 2D). Furthermore, LoX3-1.0 maintained consistent responses to individual puffs that support its stability (Figure 2E).

In addition to the temporal pattern, we also investigated whether LoX3-1.0 could depict the spatial distribution of CXCL10. Different diffusion patterns of hCXCL10 were generated through adjusting the puffing parameters and were validated by the gradient of dye. Single-cell analysis of LoX3-1.0 signals revealed global distributions of CXCL10 gradients (Figure 2F), and further quantification revealed the ability of LoX3-1.0 to distinguish gradients based on their coverage and slope (Figures 2G and 2H), supporting the subcellular spatial resolution of the sensor. Overall, the LoX3-1.0 sensor enables the precise and sensitive detection of CXCL10 across different spatiotemporal patterns.

Sensor expression does not affect major cellular physiology

We next systematically tested the effects of ectopic sensor expression on cellular physiology. We first investigated whether sensor expression leads to changes in major GPCR downstream pathways. Intracellular Ca^{2+} imaging revealed that HEK293T cells expressing LoX3-1.0 lacked a PS-induced Ca^{2+} increase, in contrast to the robust and dose-dependent Ca^{2+} signals in wild-type CXCR3-expressing cells (Figures 3A, 3B, and S3A–S3C). In a G protein complementation assay,[46] LoX3-1.0 also did not interact with $G_{\alpha i}$ proteins to generate luminescence. Notably, co-expressing LoX3-1.0 did not influence the $G_{\alpha i}$ signaling of the CXCR3 receptor expressed in the same cell (Figure 3C). Similar conclusions were drawn from biochemical detection of extracellular signal-regulated kinase (ERK) phosphorylation (Figures 3D and S3D). To test whether LoX3-1.0 couples to the arrestin pathway, we utilized an internalization assay to quantify the receptor endocytosis. Unlike CXCR3, which underwent rapid internalization (shown as intracellular puncta), the LoX3-1.0 remained stably localized at the membrane and maintained a stable fluorescence response to PS over a 6-h period (Figures 3E and S2M). Additionally, sensor expression did not affect the internalization of the CXCR3 receptor expressed in the same cell (Figure 3E). Overall, we conclude that the LoX3-1.0 sensor does not induce ectopic signal activation nor does it affect the normal signaling of the native CXCR3 receptor.

We further assessed the effect of sensor expression on T cell migration that relies on endogenous CXCR3. We isolated $CD8^+$ T cells from OT1 transgenic mice, incubated them with ovalbumin (OVA) peptide (OVA257–264, 0.01 μM) for 48 h to induce CXCR3 expression, and infected them with retroviruses expressing LoX3-1.0, LoX3-mut, or EGFP (Figure 3F). In a chemotaxis assay, we observed similar dose-dependent enrichment of three groups of $CD8^+$ T cells toward mCXCL10 (Figures 3F and 3G), suggesting that ectopic sensor expression did not affect the endogenous CXCR3-mediated cellular function. Consistently, LoX3-1.0-expressing T cells exhibited similar ERK phosphorylation induced by physiological doses of mCXCL10 when compared with mut- or EGFP-expressing cells (Figures 3H and S3E). Besides T cells, we also observed no difference in Ca^{2+} activity between neurons expressing EGFP or LoX3-1.0, including their spontaneous and high K^+-triggered activities (Figures S3F and S3G).

To guarantee the sensor reports physiologically relevant chemokine dynamics *in vivo*, we applied RNA sequencing to analyze inflammation-induced changes in *Cxcl10*-related genes. Mice

(K) Schematic (left) and traces of LoX3-1.0 to locally puffed PS (100 μM). The dashed line indicates drug application time.
(L) Quantification of the on and off rates of the sensor responses fitted with an exponential function (n = 21 cells).
Scale bars, 20 μm.
See Table S2 for statistics. See also Figures S1 and S2.

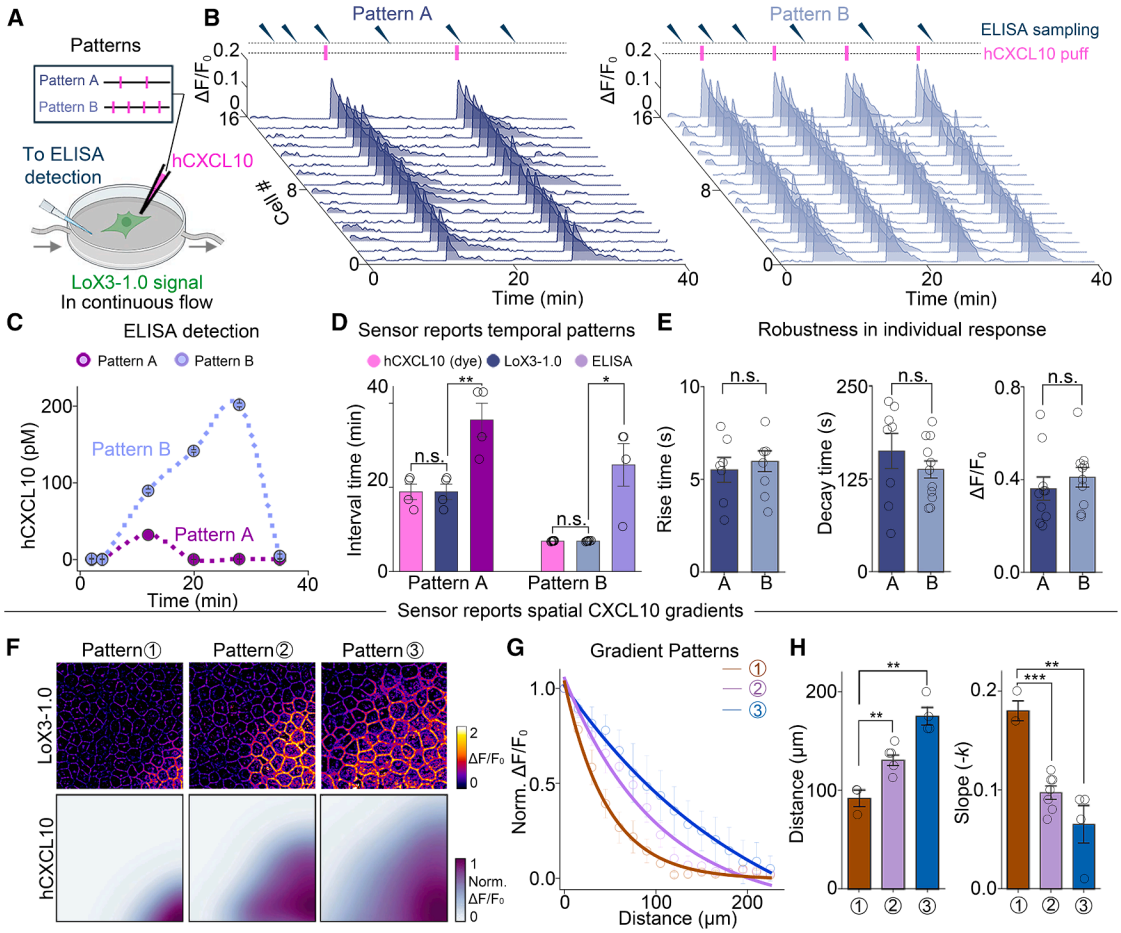

Figure 2. LoX3-1.0 captures diverse spatiotemporal patterns of CXCL10

(A) Experimental schematics in which two patterns of hCXCL10 were delivered onto LoX3-1.0-expressing cells, and the hCXCL10 in medium was sampled and measured by ELISA at selected time points.

(B) Traces of LoX3-1.0-expressing cells to two patterns of hCXCL10 (n = 16 cells). Time points of ligand application (magenta bar) and ELISA sampling (blue arrowhead) are labeled.

(C) The hCXCL10 concentration was measured by ELISA.

(D) Quantification of the peak interval of hCXCL10 mixed with dyes, changes in the fluorescence of LoX3-1.0, or the ELISA measurements of hCXCL10 (n = 4, 8 cultures for patterns A and B).

(E) Quantification of rise time (left), decay time (middle), and $\Delta F/F_0$ of LoX3-1.0 across patterns (n > 7 cultures for patterns A and B).

(F) Images showing different spatial distributions of LoX3-1.0 (up) to patterns of hCXCL10 (bottom).

(G) Normalized distribution of LoX3-1.0 signals to different hCXCL10 gradients (n = 3 cultures).

(H) Quantification of the maximum coverage (left) and decaying slope (right) of LoX3-1.0 signals across hCXCL10 patterns (n = 3, 7, and 4 cultures for patterns ①, ②, and ③).

Scale bars, 20 μm.

See Table S2 for statistics. See also Figure S2.

with hippocampal expression of LoX3-1.0 or control EGFP were subjected to either lipopolysaccharide (LPS) or saline injection (intraperitoneal [i.p.]), and tissues were collected 2 h later for transcriptional profiling (Figures 3I, up and S3H). The sensor-expressing mice showed similar expression profiles to those of the EGFP-expressing mice, suggesting no global transcriptional alteration (Figure S3I). Specifically, in both sensor- and EGFP-expressing mice, LPS injection increased the expression of proinflammatory genes (e.g., *Ccl2*, *Il1b*, and *Cxcl10*) but decreased the expression of homeostatic genes (e.g., *Sox18*) (Figure 3I, bottom, S3J, and S3K). Consistently, both EGFP- and LoX3-1.0-expressing mice showed similar LPS-dependent alteration and restitution in astrocytic and microglia reactivity *in vivo* (Figures S3L and S3M). Together, these findings support that sensor expression does not cause observable perturbations at the cellular, tissue, and organismal levels.

Chemokine dynamics exhibit multidimensional organization across immune states

As an infection progresses, the local environment and functional demands evolve, potentially requiring corresponding patterns of chemokines to encode such information. To study the spatiotemporal organization of chemokines throughout the course of infection, we mimicked various inflammatory states *in vitro*

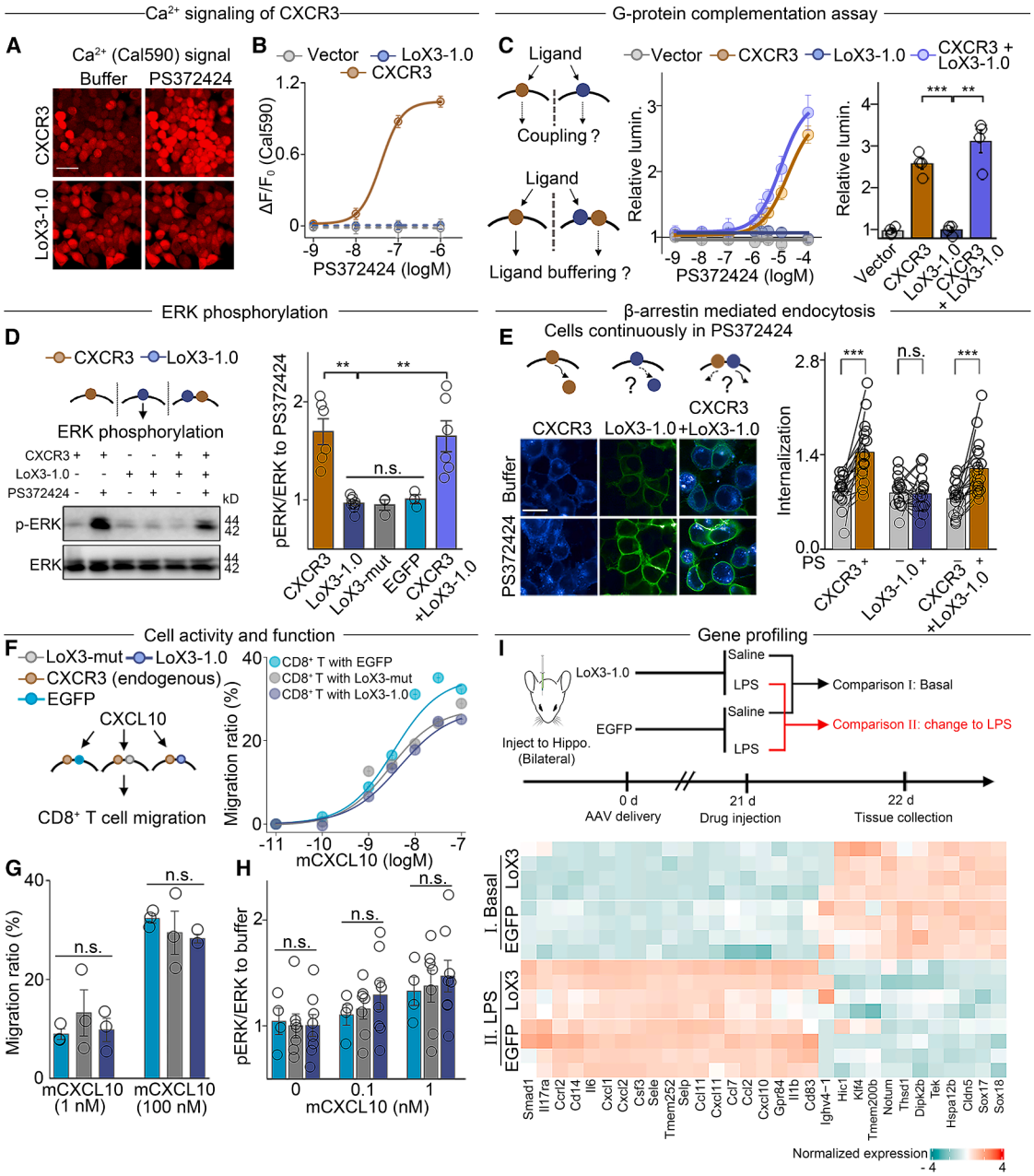

Figure 3. Negligible effects of LoX3-1.0 on cellular physiology

(A) Images showing the Ca^{2+} signal of CXCR3 (up)- or LoX3-1.0 (bottom)-expressing HEK293T cells to the application of buffer (left) or PS (1 μM, right).

(B) Ca^{2+} signals evoked by different concentrations of PS in cells expressing vector control (gray), CXCR3 (brown), or LoX3-1.0 (blue) (n = 3, 5, and 5 cultures for vector, CXCR3, and LoX3-1.0, respectively).

(C) The experimental design (left), the relative luminescence (lumin.) changes (middle), and quantification (right) in cells expressing vector (gray), CXCR3 (brown), LoX3-1.0 (blue), or co-expressing LoX3-1.0 and CXCR3 (purple) to PS application (n = 4 wells).

(D) The ERK phosphorylation in cells expressing CXCR3, LoX3-1.0, or co-expressing LoX3-1.0 and CXCR3 to buffer or PS. The raw image of LoX3-mut and EGFP is shown in Figure S3D.

(E) Left, fluorescence images of cells expressing CXCR3-BFP (blue fluorescent protein, left), LoX3-1.0 (middle), or co-expressing CXCR3-BFP and LoX3-1.0 (right) stimulated by PS (100 μM) for 1 h. Right, quantification of the fluorescence distribution (intracellular/cellular membrane) of cells in different groups (n = 19 cells).

(F) The experimental design (left) and the migration ratio (right) of LoX3-1.0- (blue), EGFP- (green), or LoX3-mut- (gray) expressing $CD8^+$ T cells to doses of mCXCL10 (n = 3 wells).

(G) Quantification of the migration ratio in $CD8^+$ T cells expressing different constructs to 1 or 100 nM mCXCL10 (n = 3 wells).

(H) Quantification of the ERK phosphorylation of $CD8^+$ T cells expressing different constructs to indicate mCXCL10 concentrations (n = 4, 7, and 8 cultures for EGFP, LoX3-mut, and LoX3-1.0, respectively).

(legend continued on next page)

from onset (O), induction (I), and effector (E) to memory (M) by stimulating HaCaT cells (a human keratinocyte cell line) with different combinations of factors and recorded the extracellular chemokine dynamics using LoX3-1.0 (Figure 4A). Compared with the control group with no observable fluorescence increase, each stimulation induced distinct patterns of LoX3-1.0 signals, indicating diverse chemokine dynamics (Figures 4B and 4C; Video S1). To confirm the signal specificity, we replaced LoX3-1.0 with LoX3-mut and observed no changes in fluorescence upon stimulation. Additionally, pretreatment with the CXCR3 antagonist or the exclusion of HaCaT cells from the system resulted in no signal increase (Figures S4A and S4B). We further applied hCXCL10 or hCXCL11 neutralizing antibodies (NAb)[47] to dissect the ligand contribution (Figures S4C and S4D). Individual application of either hCXCL10 or hCXCL11 NAb led to partial signal reduction, with their contributions depending on the total amount of chemokine, while co-application of both NAbs completely blocked the signal increase (Figure S4E), indicating that CXCL10 and 11 dominantly contribute to the signal.

The pairing between stimulatory factors and chemokine dynamics suggests both specificity and complexity in signal organization. By single-cell analysis of LoX3-1.0 response, we observed higher intra- over inter-field signal correlation that supports the biologically relevant heterogeneity across fields (Figures S4F–S4K). Therefore, the averaged field-level signals were used for unsupervised clustering, which separated the chemokine dynamics into five major patterns (Figures 4D and S5A). We further extracted functionally relevant parameters in chemokine signals and projected their values on the t-distributed stochastic neighbor embedding (t-SNE) map, which revealed the quantitative distinctions in temporal properties of chemokine. For example, pattern III exhibited early initiation but a short duration, while pattern V showed late initiation but a greater total amount (Figures 4E, 4F, and S5B). Such a multidimensional signal with a rich coding capacity would benefit signal segregation at the perceiver side. Indeed, when comparing selected chemokine patterns (e.g., III and IV) using a single dimension alone (initial time), the highly co-localized distributions suggested failure in discrimination. By contrast, including multiple signal dimensions resulted in clearer pattern separation, with more comprehensive inputs leading to better discrimination (Figures 4G, 4H, and S5C). These analyses underscore the power of LoX3-1.0 to precisely characterize the multidimensional chemokine dynamics that enable complex coding of environmental states, which might be under evaluated when only limited parameters are obtained (e.g., only detecting the amount by ELISA).

We next wonder whether complex chemokine dynamics still match specifically with the immune states. Distributional analysis revealed that each individual state was dominated by a distinct chemokine pattern (Figures 4I, S5D, and S5E). From initiation to effector states, chemokine dynamics transitioned from a rapidly initiated but transient pattern to a more robust and sustained profile. As the difference in immune states lies in the distinct combinations of immune stimuli, we further investigated the organization principle underlying state-specific chemokine signaling. A multidimensional signal can be structured in a "labeled line" manner,[48,49] where each environmental factor selectively influences a single dimension. Alternatively, multiple factors may act synergistically to shape a property at the population level. A strong and selective correlation was observed between the interferon (IFN)-γ concentration and the chemokine amount, as well as between the poly(I:C) concentration and the initial time, supporting the labeled line manner. At the same time, additional tumor necrosis factor alpha (TNF-α) coordinated with IFN-γ to extend the duration of the signal, which likely reflects population coding between highly related stimuli (Figures 4J and S5F). These diverse patterns can also be explained biologically by the regulatory pathways that control their expression (see discussion). Together, the LoX3-1.0 enables detailed dissection of chemokine dynamics following the progression of a modeled infection, underscoring the power of LoX3-1.0 to study the coding principles of chemokines as signaling molecules.

LoX3-1.0 captures cutaneous wound-induced CXCL10 release *in vivo*

To extend the application of LoX3-1.0 *in vivo*, we generated transgenic reporter mice in which LoX3-1.0 was expressed under the control of Cre recombinase (see STAR Methods). Combined with Adeno-associated virus (AAV)-mediated Cre expression in the ear skin, sensor fluorescence was clearly visualized in the dermal layer of live mice, predominantly on the plasma membrane of fibroblasts (Figures 5A–5C and S6A–S6D). Application of PS to acute LoX3-1.0-expressing ear slices led to a rapid fluorescence increase, which was blocked by pretreatment with an antagonist (Figures 5D and 5E). To induce rapid CXCL10 synthesis and release, we introduced local cutaneous wounds *in vivo* using a skin punch and conducted two-photon imaging with an enlarged field of view that included the lesion site, the wound region (W), and a control region (C) away from the lesion (Figure 5F, left). LoX3-1.0 signal exhibited a gradient distribution spanning approximately 100 μm to the wound boundary, and the response gradually increased over 9 h post-lesion and reached a plateau at 12 h and remained concentrated close to lesion sites (Figure 5F, right and S6E–S6G). As a control, mice expressing EGFP did not exhibit observable fluorescence changes to skin lesions (Figures 5G and 5H). Importantly, injection of CXCL10-NAb fully blocked the wound-induced fluorescence increase in C57BL/6J mice (which lack functional CXCL11),[50,51] supporting CXCL10 as the primary contributor (Figures 5G, 5H, S6H, and S6I). These data demonstrate that LoX3-1.0 is capable of sensitively tracking cutaneous wound-induced CXCL10 dynamics in the peripheral skin.

Distinct inflammatory states induce divergent CXCL10 temporal dynamics in the brain

To monitor the chemokine dynamics during neuroinflammation in the brain, we injected AAVs expressing LoX3-1.0 into the V1

(I) The experimental design (up) and the expression of selected inflammation-related genes (bottom) in the hippocampus of LoX3-1.0- or EGFP-expressing mice injected with saline or LPS (10 mg/kg; intraperitoneal [i.p.]) (n = 4 mice).
Scale bars, 20 μm.
See Table S2 for statistics. See also Figure S3.

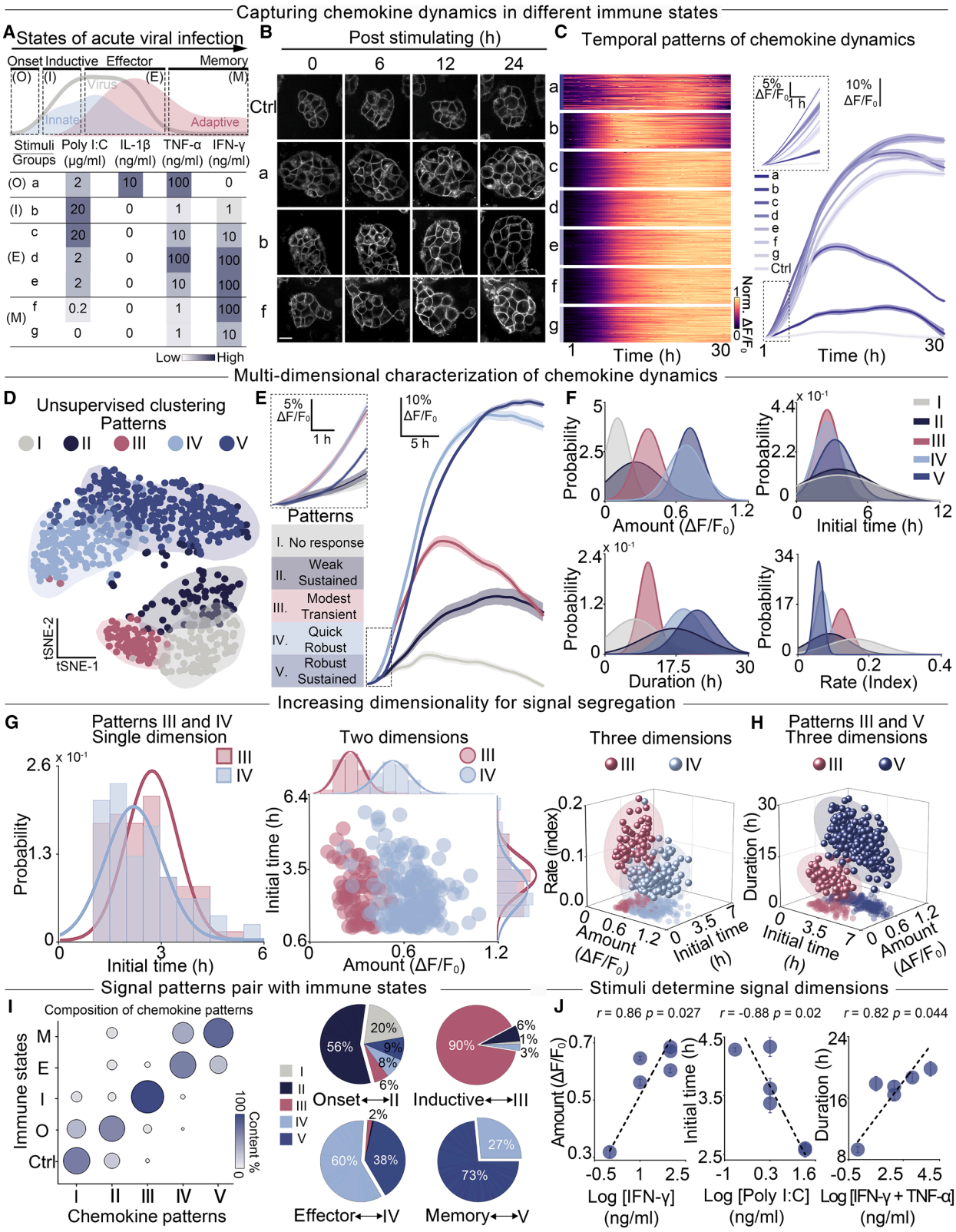

Figure 4. Multidimensional properties of chemokine signaling across immune states

(A) Experimental design to record LoX3-1.0 signals to combinations of stimulators with indicated concentrations. The dynamics of CXCR3 ligands were measured by co-cultured LoX3-1.0-expressing HEK293T cells.

(legend continued on next page)

cortex of mice and used two-photon imaging to track their signals after LPS injection (Figures 6A, S6J, and S6K). The fluorescence signal began to increase at approximately 6 h after LPS injection and then progressively reached a plateau at 18 h (Figure 6B; Video S2). As controls, saline injection or LPS injection to LoX3-mut-expressing mice all exhibited no detectable fluorescence increase. Importantly, while the CXCL9 NAb did not diminish the LPS-evoked response, it was completely blocked in CXCL10$^{-/-}$ mice (Figures 6C, 6D, S6L, S6M, and S7A), indicating that the fluorescence signal dominantly reflects the CXCL10 dynamics.

To explore chemokine dynamics in multiple immune states, we modulated the brain microenvironment by altering past infection experience, including three groups: naive (no treatment), recurrent (5 mg/kg LPS the day before), and tolerant (4 consecutive days of 0.1 mg/kg LPS). On the experimental day, all mice received 10 mg/kg LPS, and brain chemokine dynamics were recorded as described above (Figure 6E, up). LoX3-1.0 imaging revealed state-specific chemokine patterns *in vivo* that could also be explained through the extraction of signal parameters (Figures S7B and S7C; Video S3). Specifically, compared with the late onset and modest increase in the naive state, sequential high doses of LPS stimulation (recurrent) advanced the initiation and boosted the maximum amplitude of response but exhibited a rapid decline after 12 h, resulting in a shorter duration. By contrast, the tolerant state, which mimics immune memory, resulted in no significant fluorescence increase to an additional LPS challenge (Figure 6E, bottom). Normalized response of LoX3-1.0 further depicted their temporal differences between naive and recurrent status (Figure 6F). These data reflect the capability of LoX3-1.0 to capture the multidimensional properties of chemokines and their pairing with functionally relevant states *in vivo*.

Inflammation drives spatiotemporally structured CXCL10 gradients around blood vessels

Beyond temporal changes, experiments and modeling suggest that chemokines guide cellular migration mainly through spatial gradients,[52,53] yet the mapping of gradients in the functionally relevant context remains challenging. To probe the potential spatial heterogeneity of CXCL10, we analyzed the distribution of LPS-induced LoX3-1.0 signals by separating the recording field into individual 3D blocks (Figure 7A). Indeed, a clear heterogeneity of LoX3-1.0 signal was observed after LPS stimulation, while the mCherry channel did not show such differences (Figure 7B). The distribution of signal parameters also displayed multiple peaks that support signal heterogeneity (Figure 7C).

What are the potential determinants of spatial heterogeneity? We reasoned that peripherally injected LPS might affect the brain through the circulation. Thus, the location of blood vessels might be the major contributing factor. We retro-orbitally injected a fluorescent dye to label the vessel structures, allowing them to be clearly visualized simultaneously with LoX3-1.0. To further analyze the relationship between signal and the complex vessel structure, we reconstructed the vessels in 3D and assigned each pixel a vessel index (VI) reflecting its proximity to all nearby vessels (Figure S7D; see STAR Methods). When projecting block-specific CXCL10 dynamics in t-SNE, we observed a gradual change in the VI across blocks, suggesting a systematic variation in CXCL10 dynamics as a function of vessel proximity, which was absent in shuffled data (Figure S7E). Using functionally relevant parameters in LoX3-1.0 signals, including the amplitude, the T_{20} (time to 20% response), and T_{80}, we described those regions near blood vessels (with a greater VI) exhibited earlier increases, longer durations, and greater amplitudes of CXCL10 signals (Figures 7D and 7E), forming a spatiotemporal chemokine gradient beyond a static concentration profile (Figure S7F).

Finally, we tested whether we could depict the spatiotemporal evolution of LoX3-1.0 gradient across the progression of inflammation. Within the region adjacent to blood vessels, a detectable gradient emerged around 3 h after LPS injection (early phase), with limited spatial coverage and low amplitude. The gradient progressively increased in amplitude and expanded in space across 12 h (intermediate phase), with the increase in amplitude outpacing the spatial expansion, resulting in a steeper gradient and a higher signal-to-background ratio. At the late stage of inflammation (advanced phase), both the relative amplitude and spatial coverage of the gradient (above baseline) decreased, likely due to widespread inflammation throughout the parenchyma (Figures 7F, 7G, and S7G). Notably, the slope of the gradient remained stable across the intermediate to advanced phases, potentially providing continuous directional cues for cells to migrate toward the most inflamed regions (Figure 7H).

(B) Fluorescence images of LoX3-1.0 at the indicated time points in 4 typical stimulation groups.
(C) Left, the temporal dynamics of the normalized LoX3-1.0 signals in each group, with each line representing one field (n = 88 fields in each group, each field > 100 cells). Right, the average signal changes of LoX3-1.0 in each group, with the data of the initial 4 h magnified on the left (dashed region) to show differences at early phases.
(D) The t-distributed stochastic neighbor embedding (t-SNE) plot of the 5 patterns (I–V) of LoX3-1.0 signals across groups, with each dot representing one field (n = 88 fields). Unsupervised clustering is achieved by the sparse principal-component analysis (sPCA)-Gaussian mixture (GM) model (see STAR Methods).
(E) The averaged time-dependent fluorescence changes in each chemokine pattern, with the data of the first 4 h zoomed in on the left to indicate differences at early phases (n = 115, 85, 77, 163, and 264 fields for patterns I–V, respectively; each field > 100 cells).
(F) The Gaussian probability distribution of parameter values across temporal patterns.
(G) Left to right: the distribution and separation of signal patterns with a single dimension as input (left) and with two (middle) or three dimensions (right) as inputs (n = 77 and 163 fields for patterns III and IV).
(H) Similar to (G), except the comparison is made between patterns III and V with three input parameters (n = 77 and 264 fields for patterns III and V).
(I) Left, the pairing of immune states with chemokine patterns. Right, a pie graph showing the distribution of signal patterns within each immune state. The dominant pair of pattern and state is labeled below.
(J) Relationships between the stimulator concentration and signal parameters (n = 88 fields for each dot).
Scale bars, 20 μm.
See Table S2 for statistics. See also Figures S4 and S5.

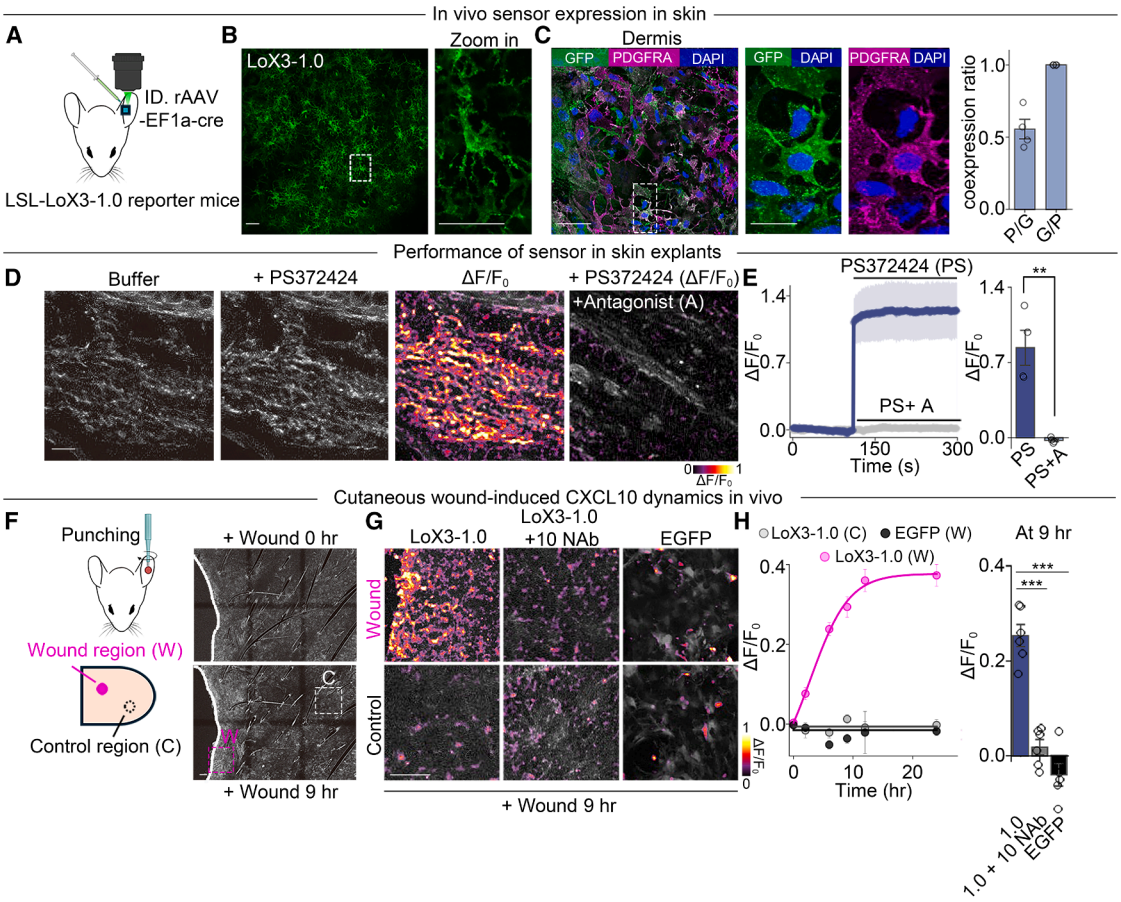

Figure 5. *In vivo* monitoring of cutaneous wound-induced CXCL10 dynamics

(A) Schematics showing the expression and imaging of LoX3-1.0 in ear skin of mice.

(B) Two-photon images of LoX3-1.0 in the ear skin *in vivo*.

(C) Immunofluorescence images of ear skin sections stained with GFP and the fibroblast marker platelet-derived growth factor receptor alpha (PDGFRA). The proportion of cells that showed the sensor (GFP) and PDGFRA signals is quantified (G, GFP; P, PDGFRA; *n* = 4 sections).

(D and E) The images (D), traces, and quantifications (E) of the fluorescence response of LoX3-1.0 in acute ear slices to the application of buffer, PS (10 μM), or a mix of PS and antagonist NBI-74330 (PS + A, both in 10 μM) (*n* = 4 slices in each group).

(F) Left, the experimental design in which the ear skin of LoX3-1.0- or EGFP-expressing mice was injured, and regions near the wound (wound region [W]) or away from the wound (control region [C]) were imaged. Right, enlarged field showing the LoX3-1.0 signal immediately after lesion (+ wound 0 h, up) or 9 h after lesion (+ wound 9 h, bottom) *in vivo*. The dashed white line indicates the wound boundary.

(G) Fluorescence response in the wound or control at 9 h after lesion in saline-injected LoX3-1.0 mice (left), mCXCL10 NAb-injected LoX3-1.0 mice (NAb, middle), or saline-injected EGFP-expressing mice (right).

(H) Left, quantification of the fluorescence changes in LoX3-1.0 or EGFP-expressing mice at different time points after injury. Right, quantification of fluorescence changes in the wound of LoX3-1.0 (1.0), LoX3-1.0 with mCXCL10 NAb (1.0 + NAb), or EGFP at 9 h after injury (*n* = 6 fields from 3 mice in each group).

Scale bars, 50 μm.

See Table S2 for statistics. See also Figure S6.

Overall, the LoX3-1.0 sensor enables precise spatiotemporal mapping of chemokine dynamics in the native context that lays the groundwork for their functional investigations.

DISCUSSION

The ability to precisely resolve intrinsic biological signals paves the way for a deeper understanding of biology. Recent advances in GPCR- and periplasmic-binding protein (PBP)-based sensors have provided powerful tools to dissect the spatiotemporal information of various extracellular signaling messengers.[54,55] Using a modular design strategy, here we developed a genetically encoded sensor for CXCR3 chemokine ligands (particularly CXCL10) and characterized its kinetics, selectivity, and biosafety across multiple systems. Similar methods that use chimeric receptor engineering have also facilitated the development of other GPCR-based sensors.[32,33,56] By employing LoX3-1.0 to track state-dependent chemokine patterns, we revealed how multidimensional properties of chemokine signaling encode environmental information over time and across space.

The expression profiling of chemokines either through sequencing or in reporter mice (e.g., REX3 mice)[57] explored the context-dependent chemokine signaling, with a focus on their intracellular synthesis as the major determinant. Beyond

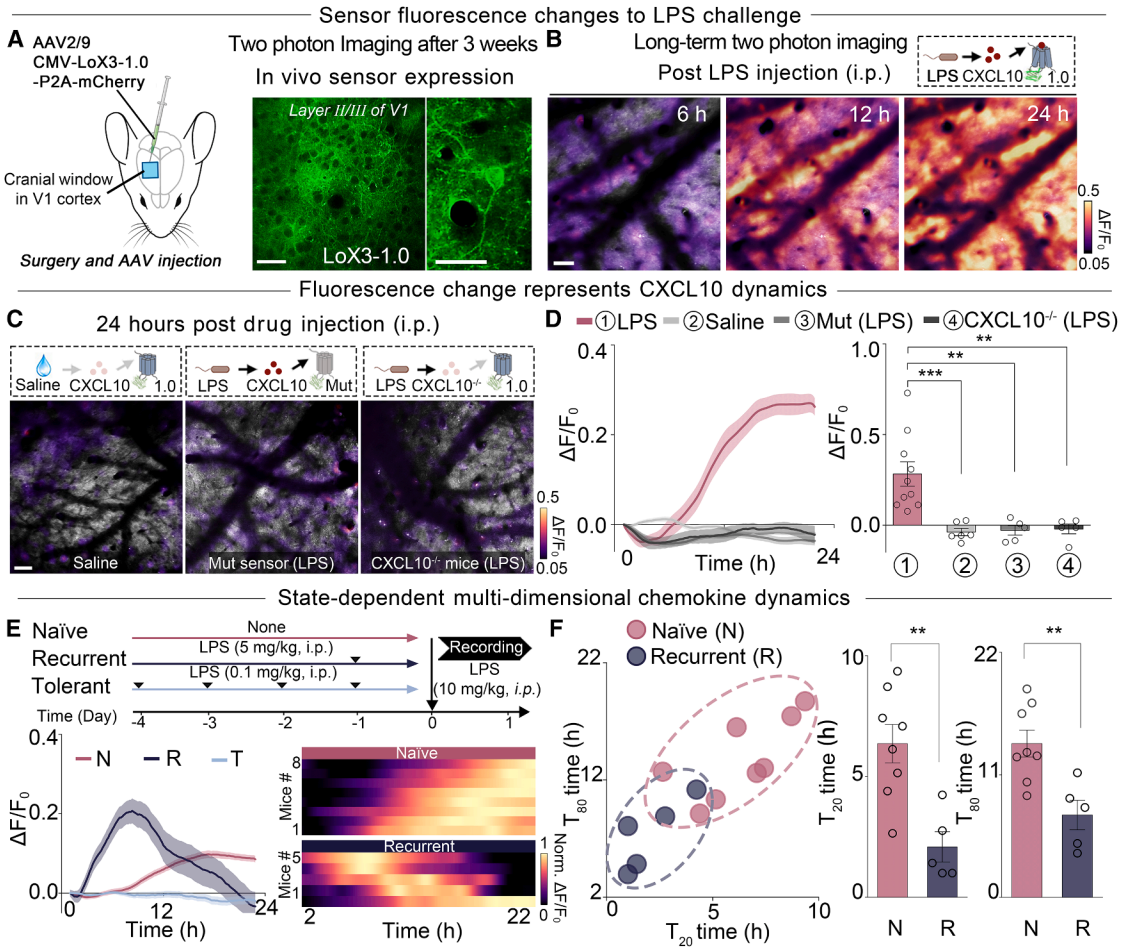

Figure 6. State-dependent *in vivo* CXCL10 dynamics during systemic inflammation

(A) Schematic and *in vivo* images of LoX3-1.0 expression in the visual cortex of mice.

(B) Images showing the fluorescence responses ($\Delta F/F_0$ in pseudocolor) of LoX3-1.0 in wild-type mice at the indicated time points after i.p. injection of 10 mg/kg LPS. The pseudocolor images are merged with the raw fluorescence images of LoX3-1.0 (in gray).

(C) Schematic (up) and representative images (bottom) showing the LoX3-1.0 signal in different groups, including saline-injected LoX3-1.0-expressing wild-type mice (left), LPS-injected LoX3-mut-expressing wild-type mice (middle), and LPS-injected LoX3-1.0-expressing CXCL10$^{-/-}$ mice (right).

(D) Left, traces of the fluorescence changes in different groups (averaged from $n = 15$ fields). Right, quantification of the average fluorescence responses between 20 and 22 h after stimulation ($n = 10$, 6, 5, and 5 mice for LPS, saline, LoX3-mut, and CXCL10$^{-/-}$, respectively).

(E) Up, the experimental procedure to create different brain immune states and record LPS-evoked CXCL10 dynamics *in vivo*. Bottom left, traces of LoX3-1.0 signals in mice with different immune states ($n = 15$ fields). Bottom right, traces of normalized LoX3-1.0 response across individual mice in the naive and recurrent states ($n = 8$ and 5 mice for naive and recurrent).

(F) Left, quantitative analysis of biologically relevant parameters in LoX3-1.0 signals, including the time to reach 20% (T_{20} time) and 80% (T_{80} time) of the maximum response. Right, quantification of parameters across states ($n = 8$ and 5 mice for naive and recurrent, respectively).

Scale bars, 40 μm.

See Table S2 for statistics. See also Figures S6 and S7.

expression, chemokines are further modulated by extracellular factors that add additional regulatory layers. The glycosaminoglycans (GAGs) in the extracellular matrix have been well documented to be indispensable for chemokine function.[25,58] However, the exact pattern of chemokines shaped by the matrix is still unclear and could vary among different chemokines.[59] We reported a CXCL10 gradient spanning ~100 μm in the skin wound model that is comparable to previously observed *in vivo* CCL21 gradients, while other works also revealed spatially distinct gradients, e.g., a broader (~600 μm) CXCL2 gradient *in vivo*, together suggesting a conserved yet context-tuned mechanism for their extracellular distribution.[60–62] In future applications, LoX3-1.0 can be either globally expressed in stomal cells to map the spatiotemporal patterns of chemokine or expressed selectively in perceiver cells to study local modulations. Although we observed no observable side effects of LoX3-1.0 on cellular physiology, future applications may need to fine-tune the expression of LoX3-1.0 to balance ligand buffering and detection sensitivity, especially when chemokines are low or localized.

Using LoX3-1.0, we revealed potential mechanisms governing chemokine signal organization that may explain their functional diversity and specificity. LoX3-1.0 mapped multidimensional

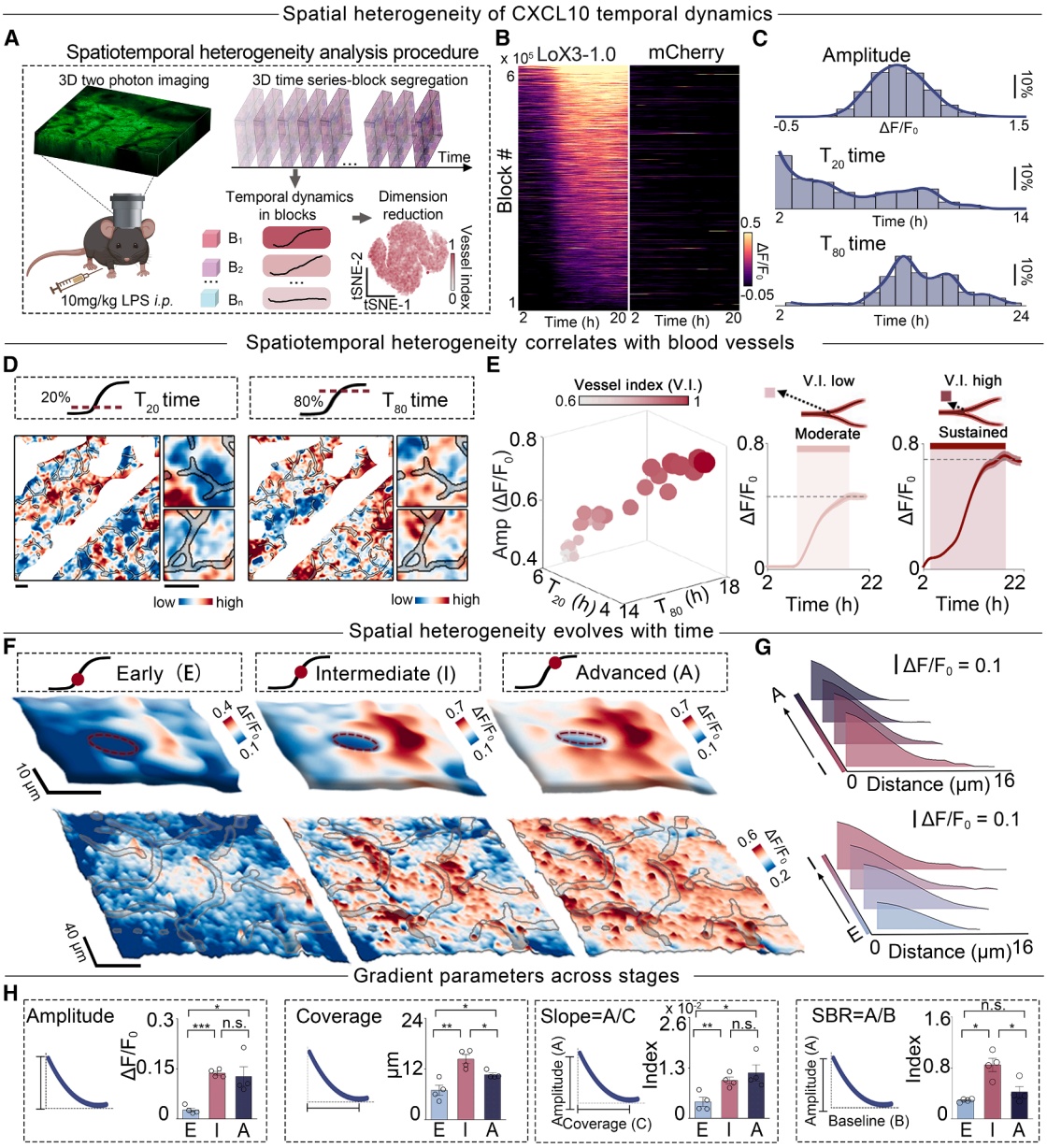

Figure 7. Micrometer-scale CXCL10 gradient and its evolution during inflammation *in vivo*

(A) Schematics of the spatial analysis of LoX3-1.0 signals and their evolution after LPS in time.

(B) Traces showing the fluorescence response in the LoX3-1.0 (left) or mCherry channel (right) in individual blocks (n = 610537 blocks; each block size = $3 \times 3 \times 3$ μm^3). The traces are sorted by the peak response of LoX3-1.0.

(C) The distribution of biologically relevant parameters of LoX3-1.0 signal across blocks.

(D) Representative images of the spatial distribution of the T_{20} time (left) or T_{80} time (right) in LoX3-1.0 signals around blood vessels (blood vessel contours are shown in black).

(E) Left, 3D scatterplot for signal parameters from blocks with different vessel indices. Right, representative traces of LoX3-1.0 in blocks with low (<0.5, left) or high (>0.9, right) vessel indices (n > 1,000 blocks).

(F) The temporal evolution of spatial gradients of LoX3-1.0 ($\Delta F/F_0$ in pseudocolor) at different inflammatory phases. The blood vessel contours are shown in gray. Regions in the dashed black blocks are magnified and shown on the top (rotated 90°) to visualize the gradient along cross-section of the blood vessel (labeled as red dashed circles).

(G) The progressional evolution of the signal gradient with time from stage E to I and from stage I to A. The response at the end of the gradient is set as the baseline.

(H) Quantification of gradient parameters at different inflammatory stages (n = 4 mice). The amplitude is defined as the maximum $\Delta F/F_0$ above the baseline, and the signal-to-background ratio is this amplitude divided by the absolute baseline $\Delta F/F_0$ value.

Scale bars, 40 μm in (D) and (F, bottom), 10 μm in (F, up).

See Table S2 for statistics. See also Figure S7.

chemokine patterns in modeled infections *in vitro* and *in vivo*, revealing how upstream signals regulate chemokine production and generate a complex yet highly structured environmental code. The distinct and state-dependent chemokine signals from keratinocytes likely reflect a sequential engagement of innate and adaptive immune signaling cascades, with rapid yet transient expression driven by interferon regulatory factor 3 (IRF3)/nuclear factor κB (NF-κB)-dependent transcription during the early innate phase, followed by delayed but sustained transcription mediated by the signal transducer and activator of transcription 1 (STAT1) during the adaptive immune responses.[63–68] Such phase-specific chemokine dynamics may orchestrate the timely recruitment and activation of immune cells for effective immune coordination, which could be further explored by combining LoX3-1.0 imaging with effector cell behaviors. In addition, these temporally resolved patterns provide a platform to deeply investigate the mechanistic basis for chemokine regulation during transitions of inflammatory stage, which may guide future interventions targeting chemokine signaling for disease treatment.

Limitations of the study

Although LoX3-1.0 captures the functional dynamics of CXCL9–11 as sensed by endogenous receptors, dissecting the dynamics of individual chemokines requires integration with genetic or pharmacological perturbations. Future mutagenesis or redesign of the ligand-binding pocket may enhance sensor selectivity toward individual ligands. While we demonstrated the ability of LoX3-1.0 to provide quantitative measurements *in vitro*, recording absolute chemokine concentrations *in vivo* remains challenging due to the difficulty of establishing standard curves, and future sensor engineering, including the implementation of lifetime-based modules, may help address this issue.

RESOURCE AVAILABILITY

Lead contact

All information and requests for further resources and reagents should be directed to and will be fulfilled by the lead contact, Miao Jing (jingmiao@cibr.ac.cn).

Materials availability

The plasmid and associated sequence information for LoX3-1.0 and LoX3-mut are available at Addgene (#234650 and #234651). The transgenic LoX3-1.0 reporter mice are available at Jackson Laboratory (#040416). Requests for other resources and reagents should be directed to and will be fulfilled by the lead contact.

Data and code availability

The source data are available in Table S2 of the manuscript. Raw data from the RNA sequencing study are publicly available for download in NCBI Sequence Read Archive (SRA): https://www.ncbi.nlm.nih.gov/sra/PRJNA1228164. All codes used in the study are available from the lead contact upon reasonable request.

ACKNOWLEDGMENTS

We thank Dr. Mo Xu at the National Institute for Biological Sciences for technical help, Dr. Wenzhi Sun and Dr. Woo-Ping Ge at the Chinese Institute for Brain Research (CIBR) for equipment sharing, and Dr. Jiahui Zhao at Peking University First Hospital for reagent sharing. Some schematics were created by BioRender. This work was supported by the STI 2030-Major Project 2021ZD0202200, subject 2021ZD0202203 (M.J.); the National Natural Science Foundation of China, grant 32371150 (M.J.); the National Key R&D Program of China, grant 2024YFA0916800 (M.J.); and the CAMS Innovation Fund for Medical Sciences (CIFMS), grant 2024-I2M-3-023 (M.J.).

AUTHOR CONTRIBUTIONS

F.X. conducted the sensor engineering and skin-related experiments with the help of L.T., and C.W. performed endogenous chemokine detection and brain-related experiments with the help of N.S. Y.W. contributed to sensor characterization. Y.C., P.L., X.G., and Q.G. contributed to imaging experiments and data analysis. D.C. contributed to T cell-related experiments under the guidance of T.C. M.J. conceived the study. F.X., C.W., and M.J. wrote the manuscript with input from all authors.

DECLARATION OF INTERESTS

The authors declare no competing interests.

STAR★METHODS

Detailed methods are provided in the online version of this paper and include the following:

- KEY RESOURCES TABLE
- EXPERIMENTAL MODEL AND STUDY PARTICIPANT DETAILS
  - Animals
  - Viruses
  - Cell lines and primary cells
- METHOD DETAILS
  - Molecular biology
  - Cell culture and cellular assays
  - Local drug administration
  - Fluorescence-activated cell sorting of primary T cells
  - T cell transduction and migration assay
  - Immunoassays
  - Western blot
  - ELISA
  - Gene expression profiling
  - Surgery, viral injection, and acute brain or ear slice preparation
  - Two-photon imaging
  - Data processing
- QUANTIFICATION AND STATISTICAL ANALYSIS

SUPPLEMENTAL INFORMATION

Supplemental information can be found online at https://doi.org/10.1016/j.immuni.2025.07.005.

Received: December 7, 2024
Revised: May 20, 2025
Accepted: July 7, 2025
Published: August 15, 2025

REFERENCES

1. Fowell, D.J., and Kim, M. (2021). The spatio-temporal control of effector T cell migration. Nat. Rev. Immunol. *21*, 582–596. https://doi.org/10.1038/s41577-021-00507-0.
2. Griffith, J.W., Sokol, C.L., and Luster, A.D. (2014). Chemokines and chemokine receptors: positioning cells for host defense and immunity. Annu. Rev. Immunol. *32*, 659–702. https://doi.org/10.1146/annurev-immunol-032713-120145.
3. Kim, C.H. (2004). Chemokine-chemokine receptor network in immune cell trafficking. Curr. Drug Targets Immune Endocr. Metabol. Disord. *4*, 343–361. https://doi.org/10.2174/1568008043339712.

4. Cyster, J.G. (1999). Chemokines and cell migration in secondary lymphoid organs. Science *286*, 2098–2102. https://doi.org/10.1126/science.286.5447.2098.

5. Harris, T.H., Banigan, E.J., Christian, D.A., Konradt, C., Tait Wojno, E.D., Norose, K., Wilson, E.H., John, B., Weninger, W., Luster, A.D., et al. (2012). Generalized Lévy walks and the role of chemokines in migration of effector CD8+ T cells. Nature *486*, 545–548. https://doi.org/10.1038/nature11098.

6. Giuliani, N., Bonomini, S., Romagnani, P., Lazzaretti, M., Morandi, F., Colla, S., Tagliaferri, S., Lasagni, L., Annunziato, F., Crugnola, M., et al. (2006). CXCR3 and its binding chemokines in myeloma cells: expression of isoforms and potential relationships with myeloma cell proliferation and survival. Haematologica *91*, 1489–1497.

7. Whiting, D., Hsieh, G., Yun, J.J., Banerji, A., Yao, W., Fishbein, M.C., Belperio, J., Strieter, R.M., Bonavida, B., and Ardehali, A. (2004). Chemokine monokine induced by IFN-gamma/CXC chemokine ligand 9 stimulates T lymphocyte proliferation and effector cytokine production. J. Immunol. *172*, 7417–7424. https://doi.org/10.4049/jimmunol.172.12.7417.

8. Yoneyama, H., Narumi, S., Zhang, Y., Murai, M., Baggiolini, M., Lanzavecchia, A., Ichida, T., Asakura, H., and Matsushima, K. (2002). Pivotal role of dendritic cell-derived CXCL10 in the retention of T helper cell 1 lymphocytes in secondary lymph nodes. J. Exp. Med. *195*, 1257–1266. https://doi.org/10.1084/jem.20011983.

9. Parent, C.A., and Devreotes, P.N. (1999). A cell's sense of direction. Science *284*, 765–770. https://doi.org/10.1126/science.284.5415.765.

10. Ebrahimzadeh, P.R., Högfors, C., and Braide, M. (2000). Neutrophil chemotaxis in moving gradients of fMLP. J. Leukoc. Biol. *67*, 651–661. https://doi.org/10.1002/jlb.67.5.651.

11. Lauffenburger, D., Farrell, B., Tranquillo, R., Kistler, A., and Zigmond, S. (1987). Gradient perception by neutrophil leucocytes, continued. J. Cell Sci. *88*, 415–416. https://doi.org/10.1242/jcs.88.4.415.

12. Vicker, M.G., Lackie, J.M., and Schill, W. (1986). Neutrophil leucocyte chemotaxis is not induced by a spatial gradient of chemoattractant. J. Cell Sci. *84*, 263–280. https://doi.org/10.1242/jcs.84.1.263.

13. Schwarz, J., Bierbaum, V., Vaahtomeri, K., Hauschild, R., Brown, M., de Vries, I., Leithner, A., Reversat, A., Merrin, J., Tarrant, T., et al. (2017). Dendritic Cells Interpret Haptotactic Chemokine Gradients in a Manner Governed by Signal-to-Noise Ratio and Dependent on GRK6. Curr. Biol. *27*, 1314–1325. https://doi.org/10.1016/j.cub.2017.04.004.

14. Petrie Aronin, C.E., Zhao, Y.M., Yoon, J.S., Morgan, N.Y., Prüstel, T., Germain, R.N., and Meier-Schellersheim, M. (2017). Migrating Myeloid Cells Sense Temporal Dynamics of Chemoattractant Concentrations. Immunity *47*, 862–874.e3. https://doi.org/10.1016/j.immuni.2017.10.020.

15. Sarris, M., and Sixt, M. (2015). Navigating in tissue mazes: chemoattractant interpretation in complex environments. Curr. Opin. Cell Biol. *36*, 93–102. https://doi.org/10.1016/j.ceb.2015.08.001.

16. Majumder, S., Zhou, L.Z., and Ransohoff, R.M. (1996). Transcriptional regulation of chemokine gene expression in astrocytes. J. Neurosci. Res. *45*, 758–769. https://doi.org/10.1002/(SICI)1097-4547(19960915)45:6<758::AID-JNR12>3.0.CO;2-S.

17. Witt, D.P., and Lander, A.D. (1994). Differential binding of chemokines to glycosaminoglycan subpopulations. Curr. Biol. *4*, 394–400. https://doi.org/10.1016/s0960-9822(00)00088-9.

18. Alanko, J., Uçar, M.C., Canigova, N., Stopp, J., Schwarz, J., Merrin, J., Hannezo, E., and Sixt, M. (2023). CCR7 acts as both a sensor and a sink for CCL19 to coordinate collective leukocyte migration. Sci. Immunol. *8*, eadc9584. https://doi.org/10.1126/sciimmunol.adc9584.

19. Boldajipour, B., Mahabaleshwar, H., Kardash, E., Reichman-Fried, M., Blaser, H., Minina, S., Wilson, D., Xu, Q., and Raz, E. (2008). Control of chemokine-guided cell migration by ligand sequestration. Cell *132*, 463–473. https://doi.org/10.1016/j.cell.2007.12.034.

20. Song, J., Wu, C., Korpos, E., Zhang, X., Agrawal, S.M., Wang, Y., Faber, C., Schäfers, M., Körner, H., Opdenakker, G., et al. (2015). Focal MMP-2 and MMP-9 activity at the blood-brain barrier promotes chemokine-induced leukocyte migration. Cell Rep. *10*, 1040–1054. https://doi.org/10.1016/j.celrep.2015.01.037.

21. Proost, P., Schutyser, E., Menten, P., Struyf, S., Wuyts, A., Opdenakker, G., Detheux, M., Parmentier, M., Durinx, C., Lambeir, A.M., et al. (2001). Amino-terminal truncation of CXCR3 agonists impairs receptor signaling and lymphocyte chemotaxis, while preserving antiangiogenic properties. Blood *98*, 3554–3561. https://doi.org/10.1182/blood.v98.13.3554.

22. Fitch, N., Marshall, S.J., Stefura, W.P., Chooniedass, R., Becker, A.B., and HayGlass, K.T. (2019). Quantifying Human Innate Cytokine and Chemokine Responses Ex Vivo via Pattern Recognition Receptor Stimulation. Methods Mol. Biol. *2020*, 77–89. https://doi.org/10.1007/978-1-4939-9591-2_6.

23. Mahajan, S.D., Schwartz, S.A., and Nair, M.P.N. (2003). Immunological assays for chemokine detection in in-vitro culture of CNS cells. Biol. Proced. Online *5*, 90–102. https://doi.org/10.1251/bpo50.

24. Venkiteswaran, G., Lewellis, S.W., Wang, J., Reynolds, E., Nicholson, C., and Knaut, H. (2013). Generation and dynamics of an endogenous, self-generated signaling gradient across a migrating tissue. Cell *155*, 674–687. https://doi.org/10.1016/j.cell.2013.09.046.

25. Sarris, M., Masson, J.B., Maurin, D., Van der Aa, L.M., Boudinot, P., Lortat-Jacob, H., and Herbomel, P. (2012). Inflammatory chemokines direct and restrict leukocyte migration within live tissues as glycan-bound gradients. Curr. Biol. *22*, 2375–2382. https://doi.org/10.1016/j.cub.2012.11.018.

26. Teleman, A.A., and Cohen, S.M. (2000). Dpp gradient formation in the Drosophila wing imaginal disc. Cell *103*, 971–980. https://doi.org/10.1016/s0092-8674(00)00199-9.

27. Heller, E.A., Liu, E., Tager, A.M., Yuan, Q., Lin, A.Y., Ahluwalia, N., Jones, K., Koehn, S.L., Lok, V.M., Aikawa, E., et al. (2006). Chemokine CXCL10 promotes atherogenesis by modulating the local balance of effector and regulatory T cells. Circulation *113*, 2301–2312. https://doi.org/10.1161/CIRCULATIONAHA.105.605121.

28. Dufour, J.H., Dziejman, M., Liu, M.T., Leung, J.H., Lane, T.E., and Luster, A.D. (2002). IFN-gamma-inducible protein 10 (IP-10; CXCL10)-deficient mice reveal a role for IP-10 in effector T cell generation and trafficking. J. Immunol. *168*, 3195–3204. https://doi.org/10.4049/jimmunol.168.7.3195.

29. Jing, M., Zhang, P., Wang, G., Feng, J., Mesik, L., Zeng, J., Jiang, H., Wang, S., Looby, J.C., Guagliardo, N.A., et al. (2018). A genetically encoded fluorescent acetylcholine indicator for in vitro and in vivo studies. Nat. Biotechnol. *36*, 726–737. https://doi.org/10.1038/nbt.4184.

30. Sun, F., Zeng, J., Jing, M., Zhou, J., Feng, J., Owen, S.F., Luo, Y., Li, F., Wang, H., Yamaguchi, T., et al. (2018). A Genetically Encoded Fluorescent Sensor Enables Rapid and Specific Detection of Dopamine in Flies, Fish, and Mice. Cell *174*, 481–496.e19. https://doi.org/10.1016/j.cell.2018.06.042.

31. Patriarchi, T., Cho, J.R., Merten, K., Howe, M.W., Marley, A., Xiong, W.H., Folk, R.W., Broussard, G.J., Liang, R., Jang, M.J., et al. (2018). Ultrafast neuronal imaging of dopamine dynamics with designed genetically encoded sensors. Science *360*, eaat4422. https://doi.org/10.1126/science.aat4422.

32. Duffet, L., Kosar, S., Panniello, M., Viberti, B., Bracey, E., Zych, A.D., Radoux-Mergault, A., Zhou, X., Dernic, J., Ravotto, L., et al. (2022). A genetically encoded sensor for in vivo imaging of orexin neuropeptides. Nat. Methods *19*, 231–241. https://doi.org/10.1038/s41592-021-01390-2.

33. Ino, D., Tanaka, Y., Hibino, H., and Nishiyama, M. (2022). A fluorescent sensor for real-time measurement of extracellular oxytocin dynamics in the brain. Nat. Methods *19*, 1286–1294. https://doi.org/10.1038/s41592-022-01597-x.

34. Kubitschke, M., Müller, M., Wallhorn, L., Pulin, M., Mittag, M., Pollok, S., Ziebarth, T., Bremshey, S., Gerdey, J., Claussen, K.C., et al. (2022). Next generation genetically encoded fluorescent sensors for serotonin. Nat. Commun. *13*, 7525. https://doi.org/10.1038/s41467-022-35200-w.

35. de Munnik, S.M., Kooistra, A.J., van Offenbeek, J., Nijmeijer, S., de Graaf, C., Smit, M.J., Leurs, R., and Vischer, H.F. (2015). The Viral G

Protein-Coupled Receptor ORF74 Hijacks β-Arrestins for Endocytic Trafficking in Response to Human Chemokines. PLoS One *10*, e0124486. https://doi.org/10.1371/journal.pone.0124486.

36. Feng, J., Zhang, C., Lischinsky, J.E., Jing, M., Zhou, J., Wang, H., Zhang, Y., Dong, A., Wu, Z., Wu, H., et al. (2019). A Genetically Encoded Fluorescent Sensor for Rapid and Specific In Vivo Detection of Norepinephrine. Neuron *102*, 745–761.e8. https://doi.org/10.1016/j.neuron.2019.02.037.

37. Rasmussen, S.G.F., DeVree, B.T., Zou, Y., Kruse, A.C., Chung, K.Y., Kobilka, T.S., Thian, F.S., Chae, P.S., Pardon, E., Calinski, D., et al. (2011). Crystal structure of the β2 adrenergic receptor-Gs protein complex. Nature *477*, 549–555. https://doi.org/10.1038/nature10361.

38. Kruse, A.C., Hu, J., Pan, A.C., Arlow, D.H., Rosenbaum, D.M., Rosemond, E., Green, H.F., Liu, T., Chae, P.S., Dror, R.O., et al. (2012). Structure and dynamics of the M3 muscarinic acetylcholine receptor. Nature *482*, 552–556. https://doi.org/10.1038/nature10867.

39. Pédelacq, J.D., Cabantous, S., Tran, T., Terwilliger, T.C., and Waldo, G.S. (2006). Engineering and characterization of a superfolder green fluorescent protein. Nat. Biotechnol. *24*, 79–88. https://doi.org/10.1038/nbt1172.

40. Shaner, N.C., Lambert, G.G., Chammas, A., Ni, Y., Cranfill, P.J., Baird, M.A., Sell, B.R., Allen, J.R., Day, R.N., Israelsson, M., et al. (2013). A bright monomeric green fluorescent protein derived from Branchiostoma lanceolatum. Nat. Methods *10*, 407–409. https://doi.org/10.1038/nmeth.2413.

41. Clark-Lewis, I., Mattioli, I., Gong, J.H., and Loetscher, P. (2003). Structure-function relationship between the human chemokine receptor CXCR3 and its ligands. J. Biol. Chem. *278*, 289–295. https://doi.org/10.1074/jbc.M209470200.

42. Jiao, H., Pang, B., Liu, A., Chen, Q., Pan, Q., Wang, X., Xu, Y., Chiang, Y. C., Ren, R., and Hu, H. (2024). Structural insights into the activation and inhibition of CXC chemokine receptor 3. Nat. Struct. Mol. Biol. *31*, 610–620. https://doi.org/10.1038/s41594-023-01175-5.

43. D'Uonnolo, G., Reynders, N., Meyrath, M., Abboud, D., Uchański, T., Laeremans, T., Volkman, B.F., Janji, B., Hanson, J., Szpakowska, M., et al. (2022). The Extended N-Terminal Domain Confers Atypical Chemokine Receptor Properties to CXCR3-B. Front. Immunol. *13*, 868579. https://doi.org/10.3389/fimmu.2022.868579.

44. Colvin, R.A., Campanella, G.S.V., Sun, J., and Luster, A.D. (2004). Intracellular domains of CXCR3 that mediate CXCL9, CXCL10, and CXCL11 function. J. Biol. Chem. *279*, 30219–30227. https://doi.org/10.1074/jbc.M403595200.

45. Cox, J.H., Dean, R.A., Roberts, C.R., and Overall, C.M. (2008). Matrix metalloproteinase processing of CXCL11/I-TAC results in loss of chemoattractant activity and altered glycosaminoglycan binding. J. Biol. Chem. *283*, 19389–19399. https://doi.org/10.1074/jbc.M800266200.

46. Wan, Q., Okashah, N., Inoue, A., Nehmé, R., Carpenter, B., Tate, C.G., and Lambert, N.A. (2018). Mini G protein probes for active G protein-coupled receptors (GPCRs) in live cells. J. Biol. Chem. *293*, 7466–7473. https://doi.org/10.1074/jbc.RA118.001975.

47. Khan, I.A., MacLean, J.A., Lee, F.S., Casciotti, L., DeHaan, E., Schwartzman, J.D., and Luster, A.D. (2000). IP-10 is critical for effector T cell trafficking and host survival in Toxoplasma gondii infection. Immunity *12*, 483–494. https://doi.org/10.1016/s1074-7613(00)80200-9.

48. Green, B.G. (2004). Temperature perception and nociception. J. Neurobiol. *61*, 13–29. https://doi.org/10.1002/neu.20081.

49. Norrsell, U., Finger, S., and Lajonchere, C. (1999). Cutaneous sensory spots and the "law of specific nerve energies": history and development of ideas. Brain Res. Bull. *48*, 457–465. https://doi.org/10.1016/s0361-9230(98)00067-7.

50. Sierro, F., Biben, C., Martínez-Muñoz, L., Mellado, M., Ransohoff, R.M., Li, M., Woehl, B., Leung, H., Groom, J., Batten, M., et al. (2007). Disrupted cardiac development but normal hematopoiesis in mice deficient in the second CXCL12/SDF-1 receptor, CXCR7. Proc. Natl. Acad. Sci. USA *104*, 14759–14764. https://doi.org/10.1073/pnas.0702229104.

51. Dalit, L., Alvarado, C., Küijper, L., Kueh, A.J., Weir, A., D'Amico, A., Herold, M.J., Vince, J.E., Nutt, S.L., and Groom, J.R. (2022). CXCL11 expressing C57BL/6 mice have intact adaptive immune responses to viral infection. Immunol. Cell Biol. *100*, 312–322. https://doi.org/10.1111/imcb.12541.

52. Jafarnejad, M., Zawieja, D.C., Brook, B.S., Nibbs, R.J.B., and Moore, J.E., Jr. (2017). A Novel Computational Model Predicts Key Regulators of Chemokine Gradient Formation in Lymph Nodes and Site-Specific Roles for CCL19 and ACKR4. J. Immunol. *199*, 2291–2304. https://doi.org/10.4049/jimmunol.1700377.

53. Hjortø, G.M., Hansen, M., Larsen, N.B., and Kledal, T.N. (2009). Generating substrate bound functional chemokine gradients in vitro. Biomaterials *30*, 5305–5311. https://doi.org/10.1016/j.biomaterials.2009.06.018.

54. Dong, C., Zheng, Y., Long-Iyer, K., Wright, E.C., Li, Y., and Tian, L. (2022). Fluorescence Imaging of Neural Activity, Neurochemical Dynamics, and Drug-Specific Receptor Conformation with Genetically Encoded Sensors. Annu. Rev. Neurosci. *45*, 273–294. https://doi.org/10.1146/annurev-neuro-110520-031137.

55. Labouesse, M.A., Cola, R.B., and Patriarchi, T. (2020). GPCR-Based Dopamine Sensors-A Detailed Guide to Inform Sensor Choice for In vivo Imaging. Int. J. Mol. Sci. *21*, 8048. https://doi.org/10.3390/ijms21218048.

56. Wang, H., Qian, T., Zhao, Y., Zhuo, Y., Wu, C., Osakada, T., Chen, P., Chen, Z., Ren, H., Yan, Y., et al. (2023). A tool kit of highly selective and sensitive genetically encoded neuropeptide sensors. Science *382*, eabq8173. https://doi.org/10.1126/science.abq8173.

57. Groom, J.R., Richmond, J., Murooka, T.T., Sorensen, E.W., Sung, J.H., Bankert, K., von Andrian, U.H., Moon, J.J., Mempel, T.R., and Luster, A. D. (2012). CXCR3 chemokine receptor-ligand interactions in the lymph node optimize CD4+ T helper 1 cell differentiation. Immunity *37*, 1091–1103. https://doi.org/10.1016/j.immuni.2012.08.016.

58. Proudfoot, A.E.I., Handel, T.M., Johnson, Z., Lau, E.K., LiWang, P., Clark-Lewis, I., Borlat, F., Wells, T.N.C., and Kosco-Vilbois, M.H. (2003). Glycosaminoglycan binding and oligomerization are essential for the in vivo activity of certain chemokines. Proc. Natl. Acad. Sci. USA *100*, 1885–1890. https://doi.org/10.1073/pnas.0334864100.

59. Graham, G.J., Handel, T.M., and Proudfoot, A.E.I. (2019). Leukocyte Adhesion: Reconceptualizing Chemokine Presentation by Glycosaminoglycans. Trends Immunol. *40*, 472–481. https://doi.org/10.1016/j.it.2019.03.009.

60. Weber, M., Hauschild, R., Schwarz, J., Moussion, C., de Vries, I., Legler, D. F., Luther, S.A., Bollenbach, T., and Sixt, M. (2013). Interstitial dendritic cell guidance by haptotactic chemokine gradients. Science *339*, 328–332. https://doi.org/10.1126/science.1228456.

61. Okada, T., Miller, M.J., Parker, I., Krummel, M.F., Neighbors, M., Hartley, S.B., O'Garra, A., Cahalan, M.D., and Cyster, J.G. (2005). Antigen-engaged B cells undergo chemotaxis toward the T zone and form motile conjugates with helper T cells. PLoS Biol. *3*, e150. https://doi.org/10.1371/journal.pbio.0030150.

62. McDonald, B., Pittman, K., Menezes, G.B., Hirota, S.A., Slaba, I., Waterhouse, C.C.M., Beck, P.L., Muruve, D.A., and Kubes, P. (2010). Intravascular danger signals guide neutrophils to sites of sterile inflammation. Science *330*, 362–366. https://doi.org/10.1126/science.1195491.

63. Handfield, C., Kwock, J., and MacLeod, A.S. (2018). Innate Antiviral Immunity in the Skin. Trends Immunol. *39*, 328–340. https://doi.org/10.1016/j.it.2018.02.003.

64. Gouwy, M., Struyf, S., Proost, P., and Van Damme, J. (2005). Synergy in cytokine and chemokine networks amplifies the inflammatory response. Cytokine Growth Factor Rev. *16*, 561–580. https://doi.org/10.1016/j.cytogfr.2005.03.005.

65. Brownell, J., Bruckner, J., Wagoner, J., Thomas, E., Loo, Y.M., Gale, M., Jr., Liang, T.J., and Polyak, S.J. (2014). Direct, interferon-independent activation of the CXCL10 promoter by NF-κB and interferon regulatory factor 3 during hepatitis C virus infection. J. Virol. *88*, 1582–1590. https://doi.org/10.1128/JVI.02007-13.

66. Bracken, R.C., Davison, L.M., Buehler, D.P., Fulton, M.E., Carson, E.E., Sheng, Q., Stolze, L.K., Guillermier, C., Steinhauser, M.L., and Brown, J.

D. (2024). Transcriptional synergy in human aortic endothelial cells is vulnerable to combination p300/CBP and BET bromodomain inhibition. iScience *27*, 110011. https://doi.org/10.1016/j.isci.2024.110011.

67. Morizane, S., Mukai, T., Sunagawa, K., Tachibana, K., Kawakami, Y., and Ouchida, M. (2023). "Input/output cytokines" in epidermal keratinocytes and the involvement in inflammatory skin diseases. Front. Immunol. *14*, 1239598. https://doi.org/10.3389/fimmu.2023.1239598.

68. Clarke, D.L., Clifford, R.L., Jindarat, S., Proud, D., Pang, L., Belvisi, M., and Knox, A.J. (2010). TNFalpha and IFNgamma synergistically enhance transcriptional activation of CXCL10 in human airway smooth muscle cells via STAT-1, NF-κB, and the transcriptional coactivator CREB-binding protein. J. Biol. Chem. *285*, 29101–29110. https://doi.org/10.1074/jbc.M109.0999952.

69. Tabatabaei, M.S., and Ahmed, M. (2022). Enzyme-Linked Immunosorbent Assay (ELISA). Methods Mol. Biol. *2508*, 115–134. https://doi.org/10.1007/978-1-0716-2376-3_10.

70. Jing, M., Li, Y., Zeng, J., Huang, P., Skirzewski, M., Kljakic, O., Peng, W., Qian, T., Tan, K., Zou, J., et al. (2020). An optimized acetylcholine sensor for monitoring in vivo cholinergic activity. Nat. Methods *17*, 1139–1146. https://doi.org/10.1038/s41592-020-0953-2.

71. Wu, Z., He, K., Chen, Y., Li, H., Pan, S., Li, B., Liu, T., Xi, F., Deng, F., Wang, H., et al. (2022). A sensitive GRAB sensor for detecting extracellular ATP in vitro and in vivo. Neuron *110*, 770–782.e5. https://doi.org/10.1016/j.neuron.2021.11.027.

72. Stringer, C., Wang, T., Michaelos, M., and Pachitariu, M. (2021). Cellpose: a generalist algorithm for cellular segmentation. Nat. Methods *18*, 100–106. https://doi.org/10.1038/s41592-020-01018-x.

73. Zou, H., Hastie, T., and Tibshirani, R. (2006). Sparse principal component analysis. J. Comp. Graph. Stat. *15*, 265–286. https://doi.org/10.1198/106186006X113430.

74. Baden, T., Berens, P., Franke, K., Román Rosón, M., Bethge, M., and Euler, T. (2016). The functional diversity of retinal ganglion cells in the mouse. Nature *529*, 345–350. https://doi.org/10.1038/nature16468.

75. Li, L., Feng, X., Fang, F., Miller, D.A., Zhang, S., Zhuang, P., Huang, H., Liu, P., Liu, J., Sredar, N., et al. (2022). Longitudinal in vivo Ca^{2+} imaging reveals dynamic activity changes of diseased retinal ganglion cells at the single-cell level. Proc. Natl. Acad. Sci. USA *119*, e2206829119. https://doi.org/10.1073/pnas.2206829119.

STAR★METHODS

KEY RESOURCES TABLE

REAGENT or RESOURCE	SOURCE	IDENTIFIER
Antibodies		
ERK1/2 Antibody	Abmart	Cat# T40071; RRID: AB_2936996
Phospho-Erk1(T202/Y204) + Erk2 (T185/Y187) Antibody	Abmart	Cat# T40072; RRID: AB_2937019
Recombinant Anti-PDGFR Alpha antibody [EPR22059-270]	Abcam	Cat# ab203491; RRID: AB_2892065
Anti-GFP antibody [9F9.F9]	Abcam	Cat# ab1218; RRID: AB_298911
Anti-Green Fluorescent Protein Antibody	Aves Labs	Cat# GFP-1010; RRID: AB_2307313
Recombinant Anti-Iba1 antibody [EPR16588]	Abcam	Cat# ab178846; RRID: AB_2636859
Chicken Anti-GFAP Polyclonal Antibody	Abcam	Cat# ab4674; RRID: AB_304558
TCR beta Monoclonal Antibody (H57-597), PE	Thermo Fisher Scientific	Cat# A15408; RRID: AB_2534421
CD45.2 Monoclonal Antibody (104), APC, eBioscience	Thermo Fisher Scientific	Cat# 17-0454-82; RRID: AB_469400
Goat Anti-Rat IgG H&L (Alexa Fluor® 647)	Abcam	Cat# ab150167; RRID: AB_2864291
Anti-Rabbit IgG H&L (Alexa Fluor 555)	Abcam	Cat# ab150078; RRID: AB_2722519
Goat Anti-Chicken IgY H&L (Alexa Fluor® 647)	Abcam	Cat# ab150171; RRID: AB_2921318
Alexa Fluor 594-AffiniPure Donkey Anti-Chicken IgY (IgG) (H+L)	Jackson ImmunoResearch Labs	Cat# 703-585-155; RRID: AB_2340377
Goat Anti-Mouse IgG H&L (Alexa Fluor® 488)	Abcam	Cat# ab150113; RRID: AB_2576208
Mouse CXCL10/IP-10/CRG-2 Antibody	R&D Systems	Cat# MAB466; RRID: AB_2292486
CXCL10 Polyclonal Antibody	Thermo Fisher Scientific	Cat# PA5-46999; RRID: AB_2609777
CXCL11 Monoclonal Antibody	Thermo Fisher Scientific	Cat# MA5-23761; RRID: AB_2610462
CXCL9 Polyclonal Antibody	Thermo Fisher Scientific	Cat# PA5-47020; RRID: AB_2609301
Mouse CXCL9/MIG Antibody	R&D Systems	Cat# AF-492-NA; RRID: AB_2086734
Bacterial and virus strains		
E. coli DH5α	CoWin Biosciences	CW0812S
AAV2/9-CMV-LoX3-1.0-P2A-mCherry	This paper	N/A
AAV2/9-CMV -LoX3-mut-P2A-mCherry	This paper	N/A
AAV2/9-CMV –EGFP	Vector core, CIBR	BV01022
AAV2/9-EF1a-Cre	Vector core, CIBR	BV06001
AAV2/9-EF1a-EGFP	Vector core, CIBR	BV01019
AAV2/9-EF1a-mCherry	Vector core, CIBR	BV01020
AAV2/9-hSyn-jRGECO1a	Vector core, CIBR	BV04014
MSCV-LoX3-1.0	VectorBuilder (This paper)	N/A
MSCV-LoX3-mut	VectorBuilder (This paper)	N/A
MSCV-EGFP	VectorBuilder (This paper)	N/A
Chemicals, peptides, and recombinant proteins		
Lipopolysaccharide (LPS)	Sigma	L4130
Fluorescein	Sigma	518-47-8
OVA peptide (257-264)	QYAOBIO	138831-86-4
I-TAC/CXCL11 protein, Human (HEK293)	MCE	HY-P7228

(*Continued on next page*)

Continued

REAGENT or RESOURCE	SOURCE	IDENTIFIER
GRO-gamma/CXCL3 protein, Human (CHO)	MCE	HY-P7192
MIP-1 alpha/CCL3 protein, Human (CHO)	MCE	HY-P7254
I-309/CCL1 protein, Human (CHO)	MCE	HY-P7198
TARC/CCL17 protein, Human (HEK293, His)	MCE	HY-P7759
HCC-4/CCL16 protein, Human (CHO)	MCE	HY-P7196
MCP-3/CCL7 protein, Human (CHO)	MCE	HY-P7240
NAP-2/CXCL7 protein, Human (CHO)	MCE	HY-P7267
ENA-78/CXCL5 protein, Human (HEK293)	MCE	HY-P7157
RANTES/CCL5 protein, Human (HEK293)	MCE	HY-P7282
PF-4/CXCL4 protein, Human (HEK293, His)	MCE	HY-P70618
MIP-3 alpha/CCL20 protein, Human (CHO)	MCE	HY-P7260
GRO-alpha/CXCL1 protein, Human (HEK293, His)	MCE	HY-P70508
CCL24/Eotaxin-2 protein, Human (HEK293, His)	MCE	HY-P7766
MCP-2/CCL8 protein, Human (HEK293, His)	MCE	HY-P7770
HCC-1/CCL14 protein, Human (HEK293, His)	MCE	HY-P7763
MPIF-1/CCL23 protein, Human	MCE	HY-P7765
Recombinant CXCL10/IP-10 protein, Human	Abcam	ab280332
Recombinant CXCL10 (N-terminal truncated, 3-77), Human	Novoprotein	CXCTX-A
Recombinant CXCL10 (C-terminal truncated, 1-73), Human	Novoprotein	CXCTX
TAK-779	MCE	HY-13406
BI-6901	MCE	HY-116835
LMD-009	MCE	HY-121885
VUF11207 fumarate	MCE	HY-110318
ML339	MCE	HY-122197
Kynurenic acid	MCE	HY-100806
CCR7 ligand 1 (Cmp2105)	MCE	HY-133073
IL-17A protein, Human (HEK293, His)	MCE	HY-P70527
IL-18 protein, Human (HEK293, His)	MCE	HY-P70760
IL-12 protein, Human (HEK293)	MCE	HY-P7032
CCR2 antagonist 4 hydrochloride	MCE	HY-103362
IL-10 protein, Human (HEK293)	MCE	HY-P70751
IL-6 protein, Human (CHO)	MCE	HY-P7044A
IFN-gamma protein, Human	MCE	HY-P7025
TNF-alpha/TNFSF2 Protein, Human	MCE	HY-P7058
IL-1 beta protein, Human	MCE	HY-P7028
Poly(I:C)	MCE	HY-107202
IFN-beta protein, Human (CHO)	MCE	HY-P73128
SB-265610	MCE	HY-50688
K777	MCE	HY-119293
AMD 3465 hexahydrobromide	MCE	HY-15971
NBI-74330	MCE	HY-15320

(*Continued on next page*)

Continued

REAGENT or RESOURCE	SOURCE	IDENTIFIER
SCH 546738	MCE	HY-10017
PS372424 hydrochloride	MCE	HY-111149A
Recombinant CXCL9, Human	Novoprotein	C437
Dextran, Alexa Fluor™ 647	Thermo Fisher Scientific	D22914
Cyanine 3.5 acid	AAT-Bioquest	147
Calbryte™ 590 AM	AAT-Bioquest	20700
ATP	MCE	HY-B2176
Serotonin hydrochloride	MCE	HY-B1473
Acetylcholine chloride	Sigma	A6625
Dopamine hydrochloride	MCE	HY-B0451A
Histamine Dihydrochloride	MCE	HY-B0722
Recombinant Mouse CXCL10 (IP-10) (carrier-free)	Biolegend	573604
Recombinant mouse CXCL9 (MIG)	MCE	HY-P70008
2-Mercaptoethanol	Thermo Fisher Scientific	21985023
Recombinant Human IL-2	Peprotech	122212
Phosphatase inhibitor cocktail II	Abcam	ab201113
Protease inhibitor cocktail	Sigma	93482
RIPA buffer	Beyotime	P0013B
Trypsin-EDTA (0.25%), phenol red	Gibco	25200056
Penicillin-Streptomycin Solution	Gibco	15140122
Fetal Bovine Serum	Gibco	A2743112CP
ACK Lysis Buffer	Beyotime	C3702
RPMI 1640 Medium	Gibco	11875093
Dulbecco's Modified Eagle Medium (DMEM)	Thermo Fisher Scientific	C11995500BT
Fibronectin(pure)	Sigma	11051407001
Poly-D-Lysine Hydrobromide	Sigma	P7280
Furimazine	Atomax	19037
Paraformaldehyde	Solarbio	P1110
Triton X-100	Sigma	X100
CellMask™ Plasma Membrane Stains	Invitrogen	C10046
Tween-20	Solarbio	T8220
Avertin	Sigma	T48402
Critical commercial assays		
Human IP-10/CXCL10 ELISA kit	NeoBioscience	EHC157.96
BCA protein assay kit	Biomed	PA101-01
Deposited data		
LoX3-1.0 and LoX3-mut plasmids	This paper	Addgene: #234650 and #234651
RNA-seq raw data	This paper	SRA: #PRJNA1228164
LoX3-1.0 reporter mice	This paper	Jackson Laboratory: #040416
Experimental models: Cell lines		
HEK293T	ATCC	RRID: CVCL_0063
LoX3-1.0 expressing stable HEK293T cell line	This paper	N/A
Human CXCL10 expressing stable HEK293T cell line	This paper	N/A
Human CXCL11 expressing stable HEK293T cell line	This paper	N/A

(*Continued on next page*)

Continued

REAGENT or RESOURCE	SOURCE	IDENTIFIER
HaCaT	Cell Resource Center, IBMS, CAMS/PUMC	1101HUM-PUMC000373
Experimental models: Organisms/strains		
Mouse: *C57BL/6J*	Jackson Laboratory	RRID: IMSR_JAX:000664
Mouse: *C57BL/6JGpt-Cxcl10^{em4Cd8736}/Gpt (Cxcl10$^{-/-}$)*	GemPharmatech	RRID: IMSR_GPT: T007446
Mouse: *C57BL/6-Tg (TcraTcrb)1100Mjb/J (OT1)*	Jackson Laboratory	RRID: IMSR_JAX:003831
Mouse: B6.C-Tg (CMV-cre)1Cgn/J	Jackson Laboratory	RRID: IMSR_JAX:006054
Mouse: *C57BL/6J-LSL-mCherry-LoX3-1.0 (LoX3-1.0 knock-in)*	This paper	N/A
Recombinant DNA		
pDisplay-CMV-LoX3-1.0-IRES-mCherry-CAAX	This paper	Addgene ID: 234650
pDisplay-CMV-LoX3-mut-IRES-mCherry-CAAX	This paper	Addgene ID: 234651
piggyBac-CAG-LoX3-1.0-IRES-mCherry-CAAX-Puro	This paper	N/A
pAAV-CMV-LoX3-1.0	This paper	N/A
pAAV-CMV-LoX3-mut-P2A-mCherry	This paper	N/A
pAAV-CMV-LoX3-1.0-P2A-mCherry	This paper	N/A
pCDNA3.1-CMV-LoX3-1.0-SmBit	This paper	N/A
pCDNA3.1-CMV-CXCR3-SmBit	This paper	N/A
pCDNA3.1-CMV-LgBit-Gαi	This paper	N/A
pDisplay-CMV-CXCR3-TagBFP-IRES-mCherry-CAAX	This paper	N/A
pDisplay-CMV-ACKR2-cpGFP-IRES-mCherry-CAAX	This paper	N/A
pDisplay-CMV-ACKR2-cpsfGFP-IRES-mCherry-CAAX	This paper	N/A
pDisplay-CMV-CCR3-cpGFP-IRES-mCherry-CAAX	This paper	N/A
pDisplay-CMV-CCR3-cpsfGFP-IRES-mCherry-CAAX	This paper	N/A
pDisplay-CMV-KSHV-GPCR-cpGFP-IRES-mCherry-CAAX	This paper	N/A
pDisplay-CMV-KSHV-GPCR-cpsfGFP-IRES-mCherry-CAAX	This paper	N/A
pDisplay-CMV-CXCR3-cpGFP-IRES-mCherry-CAAX	This paper	N/A
pDisplay-CMV-CXCR3-cpsfGFP-IRES-mCherry-CAAX	This paper	N/A
piggyBac-CAG-hCXCL10-Puro	This paper	N/A
piggyBac-CAG-hCXCL11-Puro	This paper	N/A
Software and algorithms		
Origin2018	OriginLab	https://www.originlab.com; RRID: SCR_014212
ImageJ	NIH	https://imagej.nih.gov/ij/; RRID: SCR_003070
MATLAB	MathWorks	https://www.mathworks.com/; RRID: SCR_001622
Aivia	Leica Microsystems	https://www.aiviasoftware.com/
Python 3.9	Python Software Foundation	https://www.python.org

(*Continued on next page*)

Continued

REAGENT or RESOURCE	SOURCE	IDENTIFIER
Imaris 9.7.2	Bitplane	http://www.bitplane.com; RRID: SCR_007370

EXPERIMENTAL MODEL AND STUDY PARTICIPANT DETAILS

Animals

Five- to seven-week-old C57BL/6J mice of both sexes were used for acute brain slice imaging, in vivo surgery and two-photon imaging. CXCL10 knockout mice were purchased from GemPharmatech (#T007446), and OT1 transgenic mice were purchased from Jackson Laboratory (#003831). The LSL-LoX3-1.0 reporter mice were generated by the genetic manipulation core at the Chinese Institute for Brain Research (CIBR), with the construct knocked into the H11 locus. All mice were either family-housed or pair-housed in a temperature-controlled room with a 12:12-hour light–dark cycle. All animal surgery and experimentation procedures were conducted according to protocols approved by the Animal Care & Use Committees of CIBR (#CIBR-IACUC-007). Animals were randomly assigned to treatment groups, and experiments and analyses were performed by researchers blinded to the treatment assignments.

Viruses

AAV2/9-CMV-LoX3-1.0-P2A-mCherry, AAV2/9-CMV-LoX3-mut-P2A-mCherry, AAV2/9-CMV-LoX3-1.0, AAV2/9-CMV-EGFP, AAV2/9-EF1a-Cre, AAV2/9-EF1a-EGFP, AAV2/9-EF1a-mCherry, AAV2/9-hSyn-jRGECO1a were packaged by the Vector Core at the CIBR. Retroviruses expressing EGFP, LoX3-1.0 or LoX3-mut were purchased from VectorBuilder following a standard packaging protocol. All viruses were aliquoted and stored at −80°C until use.

Cell lines and primary cells

The HEK293T cell line was originally bought from ATCC (catalog: CRL-3216) and maintained in the lab. The HaCaT cell line was purchased from the Cell Resource Center, IBMS, CAMS/PUMC (catalog: 1101HUM-PUMC000373). The stable cell lines expressing human CXCL10 or CXCL11 were constructed by co-transfection of plasmids of pyggibac-CAG-CXCL10-Puro or pyggibac-CAG-CXCL11-Puro and transposase hyPBase into HEK293T cells. 48 hours after transfection, the cells were cultured in medium containing 2 μg/mL puromycin for positive selection. Stable cell lines expressing human CXCL10 or CXCL11 were obtained after approximately one week.

To isolate primary T cells from the mouse spleen, OT-1 transgenic mice were euthanized via cervical dislocation, and their bodies were disinfected with 75% ethanol. The spleen was harvested from the left side of the body and freed from surrounding fat tissue. The spleen was placed on a 40-μm cell strainer and dissociated using a syringe plunger with 1–3 mL PBS, followed by rinsing with PBS to collect the cells into a 50 mL BD Falcon tube. Red blood cells were lysed by adding 10 mL of RBC lysis buffer for 5 minutes at room temperature. The mixture was then centrifuged at 400g for 5 minutes at 4 °C. After discarding the supernatant, the pellet was washed once with an appropriate volume of PBS, resuspended, and recentrifuged. Cells were finally resuspended in complete culture medium containing 10% FBS, 1% penicillin-streptomycin, 0.01% β-mercaptoethanol, and 10 μg/mL IL-2. Cell counting was performed before plating approximately 10^7 cells per dish in 10 mL of culture medium. For T cells used in migration assay, 10 μL of 10 μM OVA peptide was added (final concentration: 0.01 μM), and cells were cultured at 37 °C with 5% CO_2 for 48 hours before changing the medium to new one without OVA. For T cells used in fluorescence-activated cell sorting (FACS) and imaging experiments, cells were washed with PBS, resuspended, and directly subjected to fluorescent antibody staining without OVA stimulation.

METHOD DETAILS

Molecular biology

All plasmids were constructed using Gibson Assembly, with DNA fragments amplified by PCR to introduce 25–33 bp overlaps. The fragments were then assembled using T5-exonuclease (New England Biolabs), Phusion DNA polymerase (Thermo Fisher Scientific), and Taq ligase (iCloning). Plasmid sequencing was conducted by Ruibiotech and GENEWIZ. For sensor engineering and optimization, different receptors were cloned and inserted into the pDisplay vector (Invitrogen), followed by the IRES-mCherry-CAAX sequence. The fluorescent protein sequences were inserted at designated positions in the fluorescence module. Site-directed mutagenesis was performed using primers containing randomized NNB codons (48 codons in total, encoding all 20 amino acids). LoX3-1.0 and LoX3-mut were cloned and inserted into AAV vectors with the CMV promoter for *in vivo* expression, and LoX3-1.0 and LoX3-mut were cloned and inserted into the pMSCV vector for retrovirus packaging. The knock-in reporter mouse construction and related gRNA design were performed by the genetic manipulation core at the CIBR following standard CRISPR-Cas9-dependent transgene protocols.

Cell culture and cellular assays

HEK293T and HaCaT cells were cultured at 37°C in a humidified atmosphere with 5% CO_2 in DMEM (Thermo Fisher Scientific, C11995500BT), supplemented with 10% (v/v) fetal bovine serum (GIBCO, #A2743112CP) and 1% penicillin–streptomycin

(GIBCO, 15140122). HEK293T cells were transfected with NEOFECT (Neofect, #TF20121201), and experiments were performed 48 hours post-transfection. For high-content confocal imaging, cultured HEK293T cells were first plated in 96-well plates (PerkinElmer) and transfected with plasmids containing candidate sensors. Before imaging, the culture medium was replaced with Tyrode's solution containing (in mM) 150 NaCl, 4 KCl, 2 $MgCl_2$, 2 $CaCl_2$, 10 HEPES, and 10 glucose (pH 7.3-7.4). Candidates were screened using the Opera Phenix High-Content Screening System (PerkinElmer) equipped with a 40 ×/1.15 NA water-immersion objective, a 488-nm laser, and a 561-nm laser. The green and red emission bands were recorded using 525/50-nm and 600/30-nm emission filters, respectively. For sensor characterization, cells transfected with LoX3-1.0 or LoX3-mut were plated on coverslips (neuVitro, Lot # 44587819, 12 mm) and imaged by a laser scanning confocal microscope (Zeiss LSM 880). For kinetic measurements, the ligand was mixed with Cy3.5 (AAT-Bioquest, Cat#147) and added to a glass electrode (a diameter of 0.05 mm) controlled with a micro-operating system, and the medium was exchanged by perfusion to rapidly wash out the ligand. The confocal line scanning mode was used to record the fluorescence response of LoX3-1.0.

The G protein complementation assay was performed according to previous publications.[46] In brief, HEK293T cells were placed in 6-well plates and grown to 40-60% confluency. Cells were transfected by plasmids of G_i fused with large bit of nanoluc, together with LoX3-1.0 or CXCR3 fused with the small bit of nanoluc. Cells were dissociated using the cell scraper after 48 hours and resuspended in PBS solution. The samples were then placed in 96-well plates containing the substrate furimazine. Next, different concentrations of PS372424 (agonist of CXCR3; MCE, HY-111149A) were added into the well and samples were incubated for 10 minutes in dark environment, and the luminescence signals were measured by a microplate reader (TECAN).

For quantitative measurement of CXCL10 in culture using the ratiometric LoX3-1.0 sensor, a standard curve was first established by the application of known CXCL10 concentration and recorded changes in green/red signal in the same experimental system. The changes of green/red ratio of sensors to testing samples were converted to concentrations of CXCL10 according to the standard curve.

Local drug administration

To characterize sensor kinetics and create different CXCL10 temporal patterns, a local drug delivery system was used. In detail, a glass electrode was filled with solution containing PS372424, or CXCL10 with the far-red dye (1μM, Dextran-Alexa Fluor™ 647), and the electrode was connected to a pressure controller via a flexible tube. The pressure controller was set to 100 mbar and a duration of 1 s to deliver CXCL10 at frame 700/1400 in pattern A and 400/800/1200/1600 in pattern B during imaging. For spatial patterns, the pressure controller was set to 300 mbar and the duration of applied pressure was adjusted to 0.2 s, 0.4 s and 1 s for different patterns.

Fluorescence-activated cell sorting of primary T cells

T cells were suspended in 400 μL PBS at a density of 1×10^6 cells per tube and stained with TCRβ-PE (1:200) and CD45.2-APC (1:200), mixed thoroughly by pipetting, and incubated on ice for 20 min in the dark. After incubation, cells were washed by centrifugation at 400 × g for 5 min at 4°C, the supernatant was discarded, and the pellet was resuspended in 500 μL of FACS buffer (PBS with 1% FBS). The washing step was repeated once, and before flow cytometry analysis, cells were resuspended in 200 μL of FACS buffer and stained with DAPI (1:200) for viability assessment. Live cells were gated based on forward (FSC) and side scatter (SSC) profiles, and doublets were excluded using FSC-H versus FSC-A gating. Dead cells were excluded based on DAPI staining. The target cell population (TCRβ+ CD45+ T cells) was sorted using a BD FACSAria III (BD Biosciences) equipped with a 100-μm nozzle, operating at 20 psi in purity mode. Sorted cells were collected into 15-mL tubes containing RPMI 1640 with 10% FBS for T-cell imaging experiments.

T cell transduction and migration assay

Freshly isolated $CD8^+$ T cells were transduced with retroviruses expressing LoX3-1.0, LoX3-mut, or EGFP at a viral titer of 10^8 TU/mL for 48 hours. After 2–4 days of OVA treatment, cells were resuspended at 1×10^6 cells/mL, and 200 μL of the suspension was added to the upper chamber of a Transwell insert (6.5 mm, 5.0 μm pore size, Corning, #3421). The lower chamber contained 600 μL of migration buffer or mCXCL10 at a defined concentration. After incubation at 37°C, 5% CO_2 for 4 hours, cells from both chambers were collected and counted using an automated cell counter.

Immunoassays

Mouse ears were dissected at room temperature, and the epidermis and dermis were separated from the cartilage. Sections were fixed in 4% paraformaldehyde (Solarbio, Cat# P1110) for 8–10 minutes, washed with 1× PBS containing 0.3% Triton X-100 (Sigma, Cat# X100) for 15 minutes, and then blocked for 1 hour with PBS containing 1% BSA and 0.3% Triton X-100. The sections were incubated with primary antibodies (PDGFRα, Abcam, #ab203491; GFP, Abcam, #ab1218; IBA1, Abcam, #ab178846; GFAP, Abcam, #ab4674; GFP, Aveslabs, Cat#GFP-1010) diluted in blocking solution overnight at 4°C. The plasma membrane was stained using CellMask™ dye (Invitrogen, Cat#C10046). The sections were then washed with 1× PBS three times at room temperature and incubated with secondary antibodies, including goat anti-rat IgG H&L Alexa Fluor® 647 (Abcam, #ab150167), goat anti-rabbit IgG H&L Alexa Fluor® 555 (Abcam, #ab150078), Goat Anti-Chicken IgY H&L Alexa Fluor® 647(Abcam, #ab150171), donkey anti-chicken IgG H&L Alexa Fluor 594 (Jackson ImmunoResearch, #703-585-155) and goat anti-mouse IgG H&L Alexa Fluor® 488 (Abcam,

#ab150113) diluted in blocking solution for 1 hour at room temperature. Sections were washed and mounted with small drops of 50% glycerol containing 10 μg/ml DAPI. Sections were imaged with a confocal microscope (Leica TCS SP8) with a 15 μm z-stack.

Western blot

For Western blotting experiments, cells were collected and lysed with RIPA buffer (Beyotime, #P0013B) supplemented with protease inhibitor cocktail (Thermo Scientific™, #78429) and phosphatase inhibitor cocktail II (Abcam, #ab201113) to extract total protein. Total protein concentration was quantified using a BCA protein assay kit (Biomed, #PA101-01). Proteins were separated by SDS–PAGE and transferred to PVDF membranes (Millipore, #IPVH00010), which were subsequently blocked with 5% BSA in TBS containing 0.1% Tween-20 and incubated with primary antibodies, including pERK (Abmart, T40072M) and ERK (Abmart, T40071M), at 4°C overnight. The sections were then incubated with the secondary antibody goat anti-rabbit IgG H&L (HRP) (#ab6721) at room temperature for 1 hour. Signals were detected using Super ECL Detection Reagent (Thermo Scientific™, #34580) with an Invitrogen Chemiluminescent Imaging System (Invitrogen). The bands were quantified using ImageJ software (NIH).

ELISA

Samples were collected from the imaging chamber at different time points, and CXCL10 concentrations were measured using a standard sandwich ELISA (NeoBioscience, #cat EHC157.96) following similar protocols as previous publication.[69] Briefly, samples were added to the wells to bind to the capture antibody coated on the plate wells. After the addition of the capture antibody, the plate was covered and incubated at 37°C for 90 minutes. The plate was then washed 5 times with buffer. Biotinylated antibody was added to the wells and incubated for 1 hour. The plate was washed 5 times and the enzyme conjugate working solution was added to the wells and incubated for another 30 minutes. The substrate was then added to induce a color change and incubated for 15 minutes at room temperature. Finally, the reaction stop solution was added to stop the reaction. A microplate reader (TECAN) was used to measure the value of each well.

Gene expression profiling

Brain samples were dissected, total RNA was extracted, and the prepared samples were sent to Novogene (Beijing) for bulk RNA sequencing. RNA integrity was assessed using the RNA Nano 6000 Assay Kit with the Bioanalyzer 2100 system (Agilent Technologies, CA, USA). A total of 1 μg of RNA per sample was used as input material. Poly-T oligo-attached magnetic beads were used to collect the purified mRNA. First-strand cDNA was synthesized by using random hexamer primers and M-MuLV reverse transcriptase (RNase H). Second-strand cDNA synthesis was subsequently performed using DNA polymerase I and RNase H. The remaining overhangs were converted to blunt ends using exonuclease/polymerase activities. After adenylation of the 3' ends of the DNA fragments, adaptors with a hairpin loop structure were ligated to prepare for hybridization. To selectively choose 370∼420 bp cDNA fragments, the library fragments were purified with the AMPure XP system (Beckman Coulter, Beverly, USA), followed by PCR. Finally, the PCR products were purified with the AMPure XP system, and library quality was evaluated using the Agilent Bioanalyzer 2100 system. Following the manufacturer's instructions, the index-coded samples were processed on a cBot Cluster Generation System with the TruSeq PE Cluster Kit v3-cBot-HS (Illumina). After cluster generation, the library preparations were sequenced on an Illumina NovaSeq platform, generating 150 bp paired-end reads.

Surgery, viral injection, and acute brain or ear slice preparation

The surgery and viral injection followed a standard protocol, similar to previously described methods.[70,71] In brief, mice were anesthetized with an intraperitoneal (i.p.) injection of avertin (250 mg/kg body weight, Sigma–Aldrich, #T48402), and a metal head-fixed recording chamber was affixed to the skull. After 3–4 days of recovery, the mice were anesthetized and placed on a stereotaxic frame (RWD Instruments) for cranial window opening and AAV injection (400-500 nL) into the V1 visual cortex. A 4 mm × 4 mm coverslip was used to replace the skull. For transcriptomic analysis, AAVs expressing sensors or EGFP were injected into the hippocampus without cranial window opening. For skin expression, AAV encoding Cre recombinase or EGFP as controls was injected into the skin locally of LSL-LoX3-1.0 transgenic mice.

To prepare acute brain slices, mice were anesthetized with avertin after three weeks of viral injection and transcardially perfused with 5 ml of precooled slicing buffer containing (in mM) 110 choline-Cl, 2.5 KCl, 1.25 NaH_2PO_4, 25 $NaHCO_3$, 25 glucose, 7 $MgCl_2$ and 0.5 $CaCl_2$. The mice were then decapitated, and the brains were immediately removed and placed in precooled oxygenated slicing buffer (oxygenated with 95% O_2 + 5% CO_2). The brains were sectioned into 300 μm slices using a VT1200 vibratome (Leica), and the slices containing the hippocampus were immediately transferred to oxygenated ACSF containing (in mM) 125 NaCl, 2.5 KCl, 1.25 NaH_2PO_4, 25 $NaHCO_3$, 25 glucose, 1.3 $MgCl_2$ or 2 $CaCl_2$. The slices were allowed to recover at 33°C for 30 minutes before being transferred to a chamber for imaging.

For the preparation of acute ear slices, mice were anesthetized with avertin (250 mg/kg body weight; Sigma–Aldrich, #T48402), and AAVs expressing sensors or EGFP (5 μl) were intradermally injected into the left ears of the mice. Three weeks after sensor expression, the ears were immediately removed and placed in 2 ml of preheated 7% agarose buffer for fixation, and the cold-treated ears subjected to agarose gel electrophoresis were placed in precooled slicing Tyrode's solution. The ears were sectioned into 500 μm slices using a VT1200 vibratome (Leica) and transferred to the chamber (35 mm) with Tyrode's solution for two-photon imaging.

Two-photon imaging

In vivo imaging of brains of awake mice and acute brain slices was conducted using a two-photon laser-scanning microscope (FVMPE-RS; Olympus) equipped with a pulsed Ti: sapphire laser (Insight Deep See). Images were acquired using a 25× water immersion objective (XLPLN25XWMP2, 1.05 NA, Olympus). Sensors were excited at 920 nm, and its fluorescence was collected with a 495-540 nm emission filter. mCherry was excited at 1040 nm, and its fluorescence was collected with a 575-645 nm emission filter. For imaging of the LoX3-1.0 signal during inflammation, images were recorded every 10 minutes after LPS injection (Sigma, #L4130) in a 500 × 500 μm field, with Z-stack of 150 μm. To label the blood vessels in the same imaging region, the awake mice were retro-orbitally injected with 40 μL of 1% fluorescein (Sigma, # 518-47-8) after LoX3-1.0 signal recording. For imaging of the cutaneous wound model, images were acquired at the indicated time points after lesion induction with a 500 μm × 500 μm imaging field or an enlarged field of view by image stitching, and with a 100-μm Z-stack. For evaluating CXCL10 or CXCL9 contribution, the CXCL10 and 9 neutralizing antibody respectively (R&D Systems, Cat#MAB466, Cat# AF-492-NA) was intraperitoneally injected with a concentration of 50 μg/ml before two-photon imaging.

Data processing

To evaluate the performance of the sensors during screening, the ratio between green (G) and red (R) fluorescence was calculated before and after the application of ligand, and the change in the G/R ratio was used as the fluorescence response (labeled $\Delta F/F_0$). The peak G/R ratio was used as an indicator of brightness. The signal-to-noise ratio was calculated as $\Delta F/F_0$ multiplied by $\sqrt{F}$.

For in vitro analysis of chemokine dynamics at the single-cell level, HEK293T cells expressing LoX3-1.0 are identified and segmented using the Cellpose algorithm.[72] Binary whole-cell masks generated by Cellpose are eroded and then subtracted from the original masks to generate membrane masks representing regions of LoX3-1.0 expression. Membrane mask images across different time points are imported into Imaris, where they are recognized as surfaces for single-cell tracking over time. A lineage tracing algorithm is applied to analyze LoX3-1.0 responses at the single-cell level, and only tracks spanning the entire time course are retained for analysis. To ensure track continuity, a maximum gap of up to 3 frames between consecutive detections is allowed and automatically interpolated by Imaris. In cases where a single cell divides into multiple daughter cells, the chemokine signal is averaged across the daughter cells to represent the temporal dynamics of the parent cell.

For in vitro analysis of chemokine release patterns, the dimensional reduction of the LoX3-1.0 response was approximated by using a weighted sum of features with sparse coefficients. In detail, the sensor responses obtained in different experimental groups were individually normalized to their maximum response over time, and then inputted for clustering. Next, the optimal features of the sensor response were extracted by sparse principal components analysis (sPCA),[73] with the Gaussian mixture model (GMM) used to fit the distribution of sensor responses in the space of features.[74,75] The optimal number of clusters in the Gaussian functions was determined using the elbow point in the evaluation of Bayesian information criterion (BIC). For visualization, the original signal was reduced to a two-dimensional space using the t-SNE method and the different subgroups were marked with corresponding colors.

To quantify the immunostaining results of glia cells in the brain, the z-stack images were imported into Imaris software (Oxford Instruments, version 10.1.0), where microglia were identified using the Surface function and an appropriate threshold was set based on the Iba1 signal to create 3D surfaces of microglia. The volume of each microglia cell body was calculated. For GFAP signal, images were projected with maximum intensity and were processed using Aivia software for pixel classification to segment GFAP-positive areas. The voxel size of the GFAP-positive areas was calculated by the Surface function in Imaris, and the percentage of GFAP-positive area was determined by dividing the total voxel size of the GFAP-positive areas with the total voxel size of the entire field.

To register the deformation and 3D shift in the field of view (FOV) between frames during long-term *in vivo* imaging, bigstream registration (https://github.com/GFleishman/bigstream) was applied. Image volumes from each time point were registered based on the GFP (G) channel using image volume at one fixed time point as the reference, and the last frame was chosen for blood vessel-related analysis. To correct fluorescence fluctuations, mCherry (R) was used as the control channel, and changes in R channels ($\Delta F/F_0$ for R) were calculated to represent fluctuations in fluorescence. The LoX3-1.0 signal change was obtained by subtracting the change in the R channel from that in the G channel ($\Delta F/F_0$ for G). The SNR in vivo was calculated as the fluorescence response ($\Delta F/F_0$) at indicated time points post stimulation divided by the standard deviation of the baseline response.

To analyze the correlation between CXCL10 spatiotemporal dynamics and blood vessels, a three-step analysis strategy was employed: 1) Blood vessel recognition: The blood vessel structures were enhanced using the Pixel Classifier tool in Aivia 11.0.0 (Leica Microsystems, Mannheim, Germany) based on fluorescein labeling. Then, the enhanced image was used to create a binary image for a refined vessel structure via the surface tool Imaris 9.7.2 (Bitplane, South Windsor, CT, USA). 2) Vessel index generation: To quantify the correlation of blood vessels at the pixel level within the 3D volume, the kernel density estimation (KDE) approach, which is traditionally used for univariate data analysis in MATLAB (Statistics and Machine Learning Toolbox), was modified for XYZ 3D projection. The binary blood vessel image was used as the input, and the value of a Gaussian kernel function was calculated for each vessel pixel across a 3D grid, resulting in a comprehensive density estimation for the entire volume. The KDE function's bandwidth parameter was specifically set to 18 pixels to accommodate the spatial scale of vascular structures in the FOV. 3) Extraction of the temporal dynamics in spatial blocks: To capture the authentic dynamics of the signal with high spatial resolution, the size of the signal extraction unit was defined as 3 × 3 × 3 pixels to minimize the influence of minor interframe movements. The average intensity of each block was computed by convolving the original data with a uniform kernel and normalizing by the number of elements within each block, resulting in continuous signal extraction. The blocks containing pixels with no fluorescent signal were excluded.

QUANTIFICATION AND STATISTICAL ANALYSIS

The imaging data were processed using MATLAB (MathWorks) and Imaris (Oxford Instruments), and fluorescence intensity was quantified using ImageJ (National Institutes of Health). Statistical analyses were performed using MATLAB. Sample sizes are indicated for each experiment and were determined based on similar studies,[30,70,71] with no data excluded from the analysis. All data in this manuscript are reliably reproducible, and the number of replicates is indicated in the legends of the corresponding figures. Animals and cells were randomly assigned to experimental or control groups with investigators blinded to the group allocation during experiments. All group analyses are presented as the mean ± s.e.m. unless otherwise specified, with error bars representing s.e.m. For paired groups, significant differences were determined using paired Student's t-tests. For unpaired groups, an F-test was first performed to compare variances, followed by an unpaired Student's t-test. $P > 0.05$ was considered not significant (n.s.); $p < 0.05$ indicated *, $p < 0.01$ indicated **, and $p < 0.001$ indicated ***. All statistical details for the main figures are provided in Table S2.